

T. Furevik · M. Bentsen · H. Drange  
I. K. T. Kindem · N. G. Kvamstø · A. Sorteberg

## Description and evaluation of the bergen climate model: ARPEGE coupled with MICOM

Received: 28 March 2002 / Accepted: 30 December 2002 / Published online: 2 April 2003  
© Springer-Verlag 2003

**Abstract** A new coupled atmosphere–ocean–sea ice model has been developed, named the Bergen Climate Model (BCM). It consists of the atmospheric model ARPEGE/IFS, together with a global version of the ocean model MICOM including a dynamic–thermodynamic sea ice model. The coupling between the two models uses the OASIS software package. The new model concept is described, and results from a 300-year control integration is evaluated against observational data. In BCM, both the atmosphere and the ocean components use grids which can be irregular and have non-matching coastlines. Much effort has been put into the development of optimal interpolation schemes between the models, in particular the non-trivial problem of flux conservation in the coastal areas. A flux adjustment technique has been applied to the heat and freshwater fluxes. There is, however, a weak drift in global mean sea-surface temperature (SST) and sea-surface salinity (SSS) of respectively 0.1 °C and 0.02 psu per century. The model gives a realistic simulation of the radiation balance at the top-of-the-atmosphere, and the net surface fluxes of longwave, shortwave, and turbulent heat fluxes are within observed values. Both global and total zonal means of cloud cover and precipitation are fairly close to observations, and errors are mainly related to the strength and positioning of the Hadley cell. The mean sea-level pressure (SLP) is well simulated, and both the mean state and the interannual standard

deviation show realistic features. The SST field is several degrees too cold in the equatorial upwelling area in the Pacific, and about 1 °C too warm along the eastern margins of the oceans, and in the polar regions. The deviation from Levitus salinity is typically 0.1 psu – 0.4 psu, with a tendency for positive anomalies in the Northern Hemisphere, and negative in the Southern Hemisphere. The sea-ice distribution is realistic, but with too thin ice in the Arctic Ocean and too small ice coverage in the Southern Ocean. These model deficiencies have a strong influence on the surface air temperatures in these regions. Horizontal oceanic mass transports are in the lower range of those observed. The strength of the meridional overturning in the Atlantic is 18 Sv. An analysis of the large-scale variability in the model climate reveals realistic El Niño – Southern Oscillation (ENSO) and North Atlantic–Arctic Oscillation (NAO/AO) characteristics in the SLP and surface temperatures, including spatial patterns, frequencies, and strength. While the NAO/AO spectrum is white in SLP and red in temperature, the ENSO spectrum shows an energy maximum near 3 years.

---

### 1 Introduction

In the last couple of decades, satellite measurements and improved weather forecast models have provided a rapidly increasing amount of high resolution observational and reanalysis data for a wide range of variables. The most important tool in the study of present-day climate variability on annual to interdecadal time scales, and also for the study of the climate sensitivity to changes in the climate forcings such as the greenhouse gas concentrations, albedo or solar irradiance, remains the coupled atmosphere ocean general circulation model (AOGCM). As a result of insufficient computational resources and an incomplete understanding of many of the important physical processes governing our climate

---

T. Furevik (✉) · M. Bentsen · H. Drange  
Nansen Environmental and Remote Sensing Center,  
Bergen, Norway  
E-mail: tore@gfi.uib.no

T. Furevik · H. Drange · I. K. T. Kindem · N. G. Kvamstø  
A. Sorteberg  
Geophysical Institute, University of Bergen, Allégaten 70,  
5007 Bergen, Norway

M. Bentsen · H. Drange · I. K. T. Kindem · A. Sorteberg  
Bjerknes Centre for Climate Research,  
Bergen, Norway

system, simulation of present-day climate or predictions made by AOGCMs will always be affected by the wide range of approximations and parameterisations. Therefore, different models will generally not produce the same results, and new model or model concepts could possibly bring additional insight into the complex behaviour of the climate system.

In the coupled model intercomparison project (CMIP), it is generally seen that different climate variables are simulated with different skills by the different models, such that no model is nearest to the observed climate for all parameters (Lambert and Boer 2001). It is interesting to note, however, that an average over the ensemble of models provides a best overall comparison with the observations. It is difficult to assess whether this also holds for the climate predictions for the next century, but it indicates that the uncertainties in the climate scenarios may be improved by using ensemble means over a large range of different AOGCMs (Palmer 2001; Palmer and Räisänen 2002).

During recent years much attention has been paid to the atmospheric and oceanic processes taking place in the North Atlantic and the Arctic region. There are at least three reasons for this: the possible links between the strength of the thermohaline overturning circulation and rapid climate change (Rahmstorf 1995; Rahmstorf and Ganopolski 1999; Ganopolski and Rahmstorf 2001), the observed trends towards a strengthening of the westerlies (Hurrell 1995; Walsh et al. 1996), and the shrinking of the Arctic sea-ice (Johannessen et al. 1999; Rothrock et al. 1999; Wadhams and Davis 2000).

A common feature of most climate models is their rather coarse spatial resolution, and in many aspects too coarse to study the regional processes in the North Atlantic–Arctic region. In order to increase the resolution in this highly anomalous climate region of the Earth (e.g. Rahmstorf and Ganopolski 1999) we have coupled a global atmospheric model and a global ocean–sea ice model, both having the ability to use stretched grids with specified focus areas. The model system will hereafter be termed the Bergen Climate Model (BCM). The model modules in BCM are the ARPEGE/IFS general circulation model (Déqué et al. 1994), which for the first time has been coupled to a global version of the Miami Isopycnic Coordinate Ocean Model (MICOM, Bleck et al. 1992), the latter with dynamic and thermodynamic sea ice modules incorporated (Drange 1999).

In the present study we have not used the stretched version of the BCM, since an evaluation of the model in the regular mode is needed first. To test the system, we have conducted a 300-year control integration with a linear  $T_L63$  ( $2.8^\circ$ ), 31 levels resolution in the atmosphere, and approximately  $2.4^\circ \times 2.4^\circ$ , 24 levels resolution in the ocean. Key quantities of the control integration have been evaluated against available observations and compared to similar quantities from other climate models.

As the model components are well documented in the literature, only a brief description of the modules in the

BCM system will be given here (Sect. 2). Much effort has been put into handling the fluxes between the atmosphere and the ocean. This and other technical issues regarding the accuracy of the data transfers between irregular horizontal grids are discussed in Sect. 3. In Sect. 4, the model initialisation is described. The performance of the model is documented in Sect. 5. Here stability, long-term mean energy budgets and heat transports, and the mean atmosphere and ocean climate states are evaluated. In Sect. 6, the interannual to interdecadal variability are briefly discussed with focus on the El Niño – Southern Oscillation (ENSO) and North Atlantic–Arctic Oscillation (NAO/AO) patterns. Section 7 provides summary and some prospects for future experiments with the BCM.

---

## 2 Model description

### 2.1 The atmospheric component

The atmospheric model ARPEGE/IFS is a spectral model which was originally developed for weather prediction by Météo-france and ECMWF, the European Centre for Medium-Range Weather Forecasts (Courtier et al. 1991), and later extended to a climate version by Déqué et al. (1994). Descriptions of later model improvements can be found in Déqué and Piedelievre (1995) and Déqué et al. (1998). We will here only give a brief outline of the model.

The ARPEGE/IFS is a spectral model with semi-Lagrangian two-time level integration. This scheme provides a doubling of efficiency as compared with a three-time level leapfrog scheme. Semi-Lagrangian formulation also gives the opportunity to use a linear grid for discrete computations. As the number of grid points are smaller in the linear grid than in the more common quadratic grid, this saves additional computational costs (Hortal 1998). In this study we use a spectral truncation of wave number 63, linear grid and a time step of 1800s. The linear  $T_L63$  grid has the same number of points as the quadratic T42 grid.

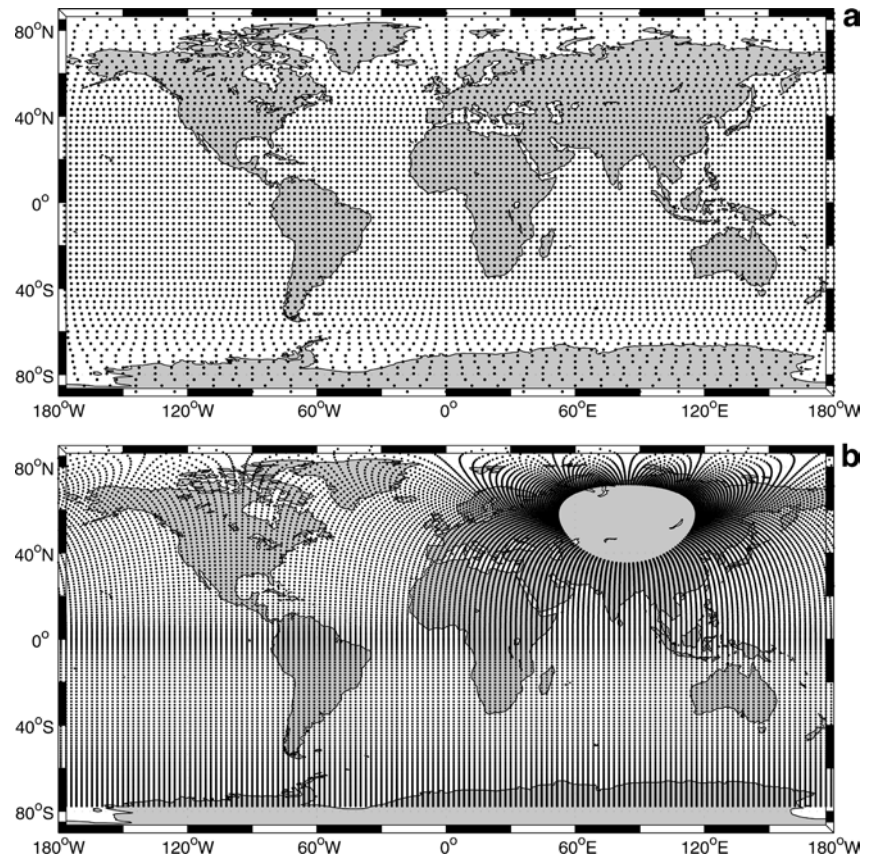
The hydrostatic Navier-Stokes equations govern the evolution of the atmospheric flow by ensuring conservation of mass, energy and momentum. The acceleration of gravity depends on latitude and height. The model atmosphere is a mixture of air, water vapour and an optional number of dynamically passive constituents. One of these is ozone, which is simulated using an Eulerian advection scheme. This option has been turned off in the present integration.

The energy sources and sinks in the equation system described arise from discretisation and horizontal diffusion. Sources and sinks due to small-scale physical processes are parameterised. The grid-boxes are defined by the computational grid, consisting of the points at which the non-linear terms in the Navier Stokes equations are calculated (linear grid). This is a latitude/longitude grid, which in the  $T_L63$  case has 64 nearly equidistant latitudes. The reduction of the grid near the poles (Hortal and Simmons 1991) gives approximately uniform horizontal resolution. The horizontal grid distribution is shown in Fig. 1a.

The vertical hybrid coordinate (Simmons and Burridge 1981) follows the topography in the lower troposphere, but becomes gradually parallel to pressure surfaces with increasing height. For the experiments presented here, we apply 31 model levels, ranging from the surface to 10 hPa. Spurious reflection at the model top is avoided through strong horizontal diffusion in the top model layers.

The physical parameterisation is divided into several explicit schemes, which in turn calculate the flux of mass, energy and/or momentum due to a specific physical process. The physical parameterisation schemes in ARPEGE were originally taken from

**Fig. 1** The horizontal grid distribution for **a** the atmosphere and **b** ocean



the climatic version of Météo-France's EMERAUDE model, described in Coiffier et al. (1987). Different schemes employed in the present version of ARPEGE and relevant references are listed in Table 1.

Unlike the model description in Déqué et al. (1998), the particular version used in BCM contains a convective gravity-wave drag parameterisation (Bossuet et al. 1998), a new snow scheme (Douville et al. 1995), an increase of the orographic wave drag (Lott 1999) and modifications in deep convection and soil vegetation schemes. Data for boundary conditions employed by the ARPEGE model are listed in Table 2.

## 2.2 The ocean component

The main features of the ocean model MICOM are described in Bleck et al. (1992). On top of a stack of isopycnic layers a non-isopycnic surface mixed layer provides the linkage between the atmospheric forcing and the ocean interior. The turbulent kinetic

energy closure for the mixed layer was originally based on the Kraus and Turner (1967) bulk formulation, but in the current version of the model the Gaspar (1988) formulation is used.

In the original version of MICOM, salinity is chosen as a prognostic variable in the isopycnic layers, while temperature is derived from the equation of state. This means that only salinity is advected and diffused in the model layers. For the advection part, this approach is consistent with solving the advection equation for

**Table 2** Boundary data employed in ARPEGE

Condition	Source
Orography	US Navy data
Vegetation roughness length	Mahfouf et al. (1995)
Land ice extent, vegetation, surface emissivity	CLIMAP 1981
Albedo	Geleyn and Preuss (1983)

**Table 1** Parametrisation schemes employed in ARPEGE

Parameterisation type	Reference
Surface	Mascart et al. (1995)
Turbulence	Louis (1979); Geleyn (1988); Richard and Royer (1993)
Shallow convection	Geleyn (1987)
Radiation	Morcrette (1991)
Convection	Bougeault (1985)
Ozone	Cariolle and Déqué (1986)
Gravity wave drag	Déqué et al. (1994); Lott and Miller (1997); Lott (1999)
Mesospheric drag	Déqué et al. (1994)
Soil and snow	Noilhan and Planton (1989); Mahfouf et al. (1995); Douville et al. (1995); Boone et al. (2000)
Clouds and precipitation	Richard and Royer (1993); Déqué et al. (1994)

temperature. One problem, however, is that the diagnosed temperature is extremely sensitive to small salinity variations in cold and fresh waters. To circumvent potential problems at high latitudes, temperature was chosen as the prognostic variable in BCM. Furthermore, salinity and temperature, and not the default choice of salinity and potential density, are used as the prognostic variables in the ocean mixed layer.

The layer thickness diffusion in MICOM was originally handled by Laplacian diffusion of layer interfaces. The diffusivity needed with this scheme to sufficiently dampen out grid-scale noise leads to unrealistic layer structure with large-scale interface features being smeared out. A biharmonic interface diffusion scheme was therefore implemented and applied in this study. This scheme has a special treatment of massless layer interfaces to avoid unrealistic interface diffusion near the bottom and near the base of the mixed layer.

In order to configure MICOM to a wide variety of applications, metric scale factors in both lateral directions have been included. The model can then easily be configured on a general orthogonal grid as described by Gal-Chen and Somerville (1975).

To avoid grid singularities in the computational ocean domain Bentsen et al. (1999), one pole is located over central Siberia while the other is at the South Pole (Fig. 1b). The resulting ocean grid configuration is, for comparison, quite similar to the one presented in Madec and Imbard (1996). With the exception of the equatorial region and near the poles, the ocean grid is almost regular, with horizontal grid spacing approximately  $2.4^\circ \times 2.4^\circ$ . In order to better resolve the dynamics near the equator, the horizontal spacing in the meridional direction is gradually reduced to  $0.8^\circ$  along the equator. In the vertical, the ocean model has 24 layers, with potential densities relative to the surface ranging from  $\sigma_\theta = 23.54$  to  $\sigma_\theta = 28.10$ . Recently, Sun et al. (1999) modified MICOM to include the effect of thermobaricity, however, this is not included in this study. Over the open ocean, the albedo is depending on the distribution of the diffusive and direct shortwave solar radiation, with a constant value (0.065) for the diffusive part and a solar zenith angle dependency for the direct part. The latter uses a simple functional fit to the albedo measurements given by Payne (1972).

### 2.3 The sea-ice component

In the present version of BCM, the sea-ice model is an integrated part of the ocean model. The ocean–sea ice module share the same grid, and the heat, salt and water fluxes among them are handled in an internally consistent way. The thermodynamic part of the sea-ice model follows Drange and Simonsen (1996), and is based on the thermodynamics of Semtner (1976), Parkinson and Washington (1979) and Fichefet and Gaspar (1988). The dynamic part of the model is based on the viscous-plastic rheology of Hibler (1979) with the modifications and implementation of Harder (1996). Over sea-ice, the albedo depends on whether the ice is snow covered or not, whether it is freezing or melting, and on the thickness (age) of the sea ice (Drange and Simonsen 1996). Typical values for respectively ice and snow are 0.80 and 0.85 in the freezing season, and 0.60 and 0.70 in the melting season. A description of how the surface temperatures of the sea-ice are computed, is included in Appendix 1.

### 2.4 The coupler

The OASIS (Ocean Atmosphere Sea Ice Soil) coupler has been used to couple the atmosphere and ocean models. It was developed at the National Centre for Climate Modelling and Global Change (CERFACS), Toulouse, France (Terray and Thual 1995; Terray et al. 1995), and is currently in use in many climate centres, among them the ECMWF, Max Plank Institute (MPI) and CERFACS (e.g., Guilyardi and Madec 1997; Cassou et al. 1998; Barthelet et al. 1998). In BCM, OASIS version 2.2 (Terray et al. 1998) is used.

The main tasks of OASIS are to synchronise the models, so the fastest running model can wait for the other model until they are both integrated over a prescribed time interval (24 h), and to read

the exchange fields from the source model, apply weight coefficients for the interpolations, and finally write the new fields to the target model.

## 3 Data transfers between irregular grids

In BCM, the two model components exchange data once every day. A total number of 15 fields are either exchanged between the models, or used internally in OASIS to modify the interpolation of other fields. The SST, sea-ice cover and albedo are passed from the ocean to the atmosphere. In return, the atmospheric model gives the heat fluxes (divided into the non-solar and the solar components), the fresh-water fluxes (evaporation, rain, snow and runoff), the momentum fluxes (zonal and meridional components), total cloud cover (used in the albedo calculations of the ocean model), and the non-solar heat flux dependency on the temperature (used in the subgrid interpolation, Sect. 3.3, and in the sea-ice model, Appendix 1). In addition, the atmospheric model passes surface temperature and albedo to OASIS, which are used to modify the heat fluxes by the subgrid method described in Sect. 3.3.

### 3.1 Exact mapping

For AOGCMs, it is common to apply either identical grids (Russell et al. 1995; Miller et al. 1996; Roeckner et al. 1996; Gordon and O'Farrell 1997; Johns et al. 1997) or grids where each atmospheric cell is exactly divided into an integer number of ocean grid cells, and where both models use the same (coarse) coastline (Mantoura et al. 1991; Flato et al. 2000; Gordon et al. 2000).

In the BCM system, both the atmosphere and ocean components can be on irregular, non-uniform grids with non-matching coastlines. This makes it possible to utilise the generally higher horizontal grid resolution in the ocean component, or to focus both models in independent geographical areas. However, to achieve a physically correct exchange of fields between two grids having irregular shapes and non-matching coastlines, is not a trivial problem.

In the BCM, the mapping between the atmosphere and ocean grids has been determined in the following way: common areas between grid cells in the two models are identified by a Monte-Carlo method. A large number (here  $25 \times 10^9$ ) of random geographical positions on the Earth are generated, and the corresponding grid positions in the atmosphere and ocean models are found. The results are tabulated such that for every atmospheric grid cell, there is information on the number of hits ( $n_i$ ) in each of the oceanic grid cells, and vice versa. By dividing by the total number of hits in each atmospheric grid cells, the fraction of an atmospheric grid cell contained in each of the ocean grid cells becomes  $n_i / \sum n_i$ .

It is now possible to achieve area-weighted mappings between the grids, here termed exact mapping, to a high degree of accuracy. This method works on any grid configuration, and is used only once prior to the start of the coupled integration. The tabulated results are then archived and retrieved prior to each interpolation.

### 3.2 Land–sea mismatch

In order to achieve an optimal interpolation between the different grids, special attention must be paid to the four cases where atmospheric sea points can partly or entirely overlay ocean land points, or where atmospheric land points can partly or entirely overlay ocean sea points.

For atmospheric sea points being only partly above ocean sea points, the SST, sea-ice cover and sea-surface albedo are calculated using the ocean sea points only. Climatological values of SST, sea ice, and albedo are used for atmospheric sea points entirely above ocean land points, as is the case for several inland seas and also further south in the Weddell Sea. Interpolation or extrapolation

from the nearest sea points in the ocean model would otherwise have given physically unrealistic values, as an inland sea typically experiences much larger seasonal cycles in the climate parameters than do open ocean areas.

Exact mapping interpolates local heat and fresh-water fluxes correctly between the grids, but the area-integrated fluxes will generally not be conserved due to the differences in the land and sea areas in the two model components. Without horizontal advection of heat or atmospheric moisture in the models, this would not be a problem as the errors in the area-integrated values of e.g. the solar and non-solar heat fluxes cancel. To ensure regional conservation of the fluxes, the weight files produced by the Monte-Carlo method (Sect. 3.1) are modified. Thus, the first step is to use exact mapping on all heat and fresh-water fluxes. Secondly, excess fluxes from atmospheric sea points partly overlying ocean land points are distributed uniformly onto the nearby ocean area, so the area-integrated flux is conserved. Locally there may be a small difference between the fluxes given by the atmosphere and the fluxes received by the ocean. Correspondingly, ocean sea points partly or entirely below atmospheric land points are given the flux produced by the overlying or nearby atmospheric sea points respectively, and the same area-integrated value is subtracted from nearby ocean areas. Again this method ensures regional conservation of the fluxes.

For the momentum flux, we have applied a bicubic interpolation, as an exact mapping from a coarse resolution atmospheric grid to a finer resolution ocean grid would have produced areas with successively no curl and areas with physically unrealistic large curl. In this case no attention has been paid to the land–sea mismatch, so the momentum fluxes given to the ocean model in the coastal areas may be affected by the atmospheric land points.

For the interpolation of the scalar fields from the atmosphere to the ocean, we have applied exact mapping from the atmospheric sea points only. For cases where ocean sea points were entirely below atmospheric land points, a Gaussian interpolation from the eight nearest atmospheric sea points were used.

### 3.3 Subgrid interpolation

In contrast to the atmosphere, the ocean contains a range of small-scale dynamical structures that are important for the large-scale circulation. Thus the ocean model needs a much higher resolution than the atmosphere if it shall be able to respond adequately to the given atmospheric forcing. In coupled models, the grid spacing is therefore generally smaller in the ocean part of the system than in the atmospheric part. To utilise the higher resolution in the ocean, we use a technique known as subgrid interpolation for the non-solar and solar heat fluxes (Terray et al. 1998): For the non-solar heat flux received by the ocean  $Q_{ns,i}$ , the flux is based on the expression

$$Q_{ns,i} = Q_{ns} + \frac{\partial Q_{ns}}{\partial T} (T_i - T), \quad (1)$$

where  $Q_{ns}$ ,  $T$ , and  $\partial Q_{ns}/\partial T$  are respectively the non-solar heat flux, the SST, and the heat flux dependency on SST on the atmospheric grid, and  $T_i$  is the SST on the ocean grid. For the solar heat flux  $Q_{sw,i}$  received by the ocean, the flux is weighted according to the surface albedo by

$$Q_{sw,i} = \frac{1 - \alpha_i}{1 - \alpha} Q_{sw}, \quad (2)$$

where  $Q_{sw}$  and  $\alpha$  are respectively the solar heat flux and albedo on the atmospheric grid, and  $\alpha_i$  is the albedo on the ocean grid.

Without the subgrid interpolation, neighbouring ocean grid cells having different properties will receive or lose the same amount of energy, which will be particularly unrealistic where temperature gradients, ice edges, or coastlines are present.

### 3.4 Runoff

To avoid an unrealistic drift of surface salinity, a balanced fresh-water budget is required. The balance between ice and water is taken care of by the ice model, and the balance between the

atmosphere and the ocean is generally solved by the atmospheric model. Over the continents the atmospheric model stores fresh-water temporarily in two reservoir layers of soil moisture and one snow reservoir. The residual, when summing up precipitation, evaporation and temporal storage of surface water in an atmospheric grid cell, is available for freshwater runoff. To balance the freshwater budget, the runoff should be discharged into the ocean. The challenge is to put the runoff produced by the atmosphere model into the appropriate discharge catchments and finally into the corresponding coastal ocean grid cells.

The Total Runoff Integrating Pathways (TRIP) data set (Oki and Sud 1998) covers the entire globe and parameterises the out-flow direction for each land grid point at a resolution of  $1^\circ \times 1^\circ$ . An automatic procedure, using the TRIP data set has been implemented to assign each land point in the atmospheric model to discharge points along the coast in the ocean model. This information is used by the coupler to exchange the runoff directly to the coastal points in the ocean models.

The runoff is distributed to the ocean independently of the initial distance from the coast and topography and land characteristics along the pathway. Intense short-term precipitation over a drainage basin may therefore lead to an unrealistic peak of freshwater input to the actual discharge points corresponding to the drainage basin, and to physically unrealistic salinity values in the oceanic mixed layer. To avoid this, the freshwater discharge is smoothed in a conservative manner by storing the runoff in a reservoir which is drained by an e-folding time scale of seven days. This e-folding scale may be unrealistically short for many river systems, but it was found sufficiently large to avoid the problems described above.

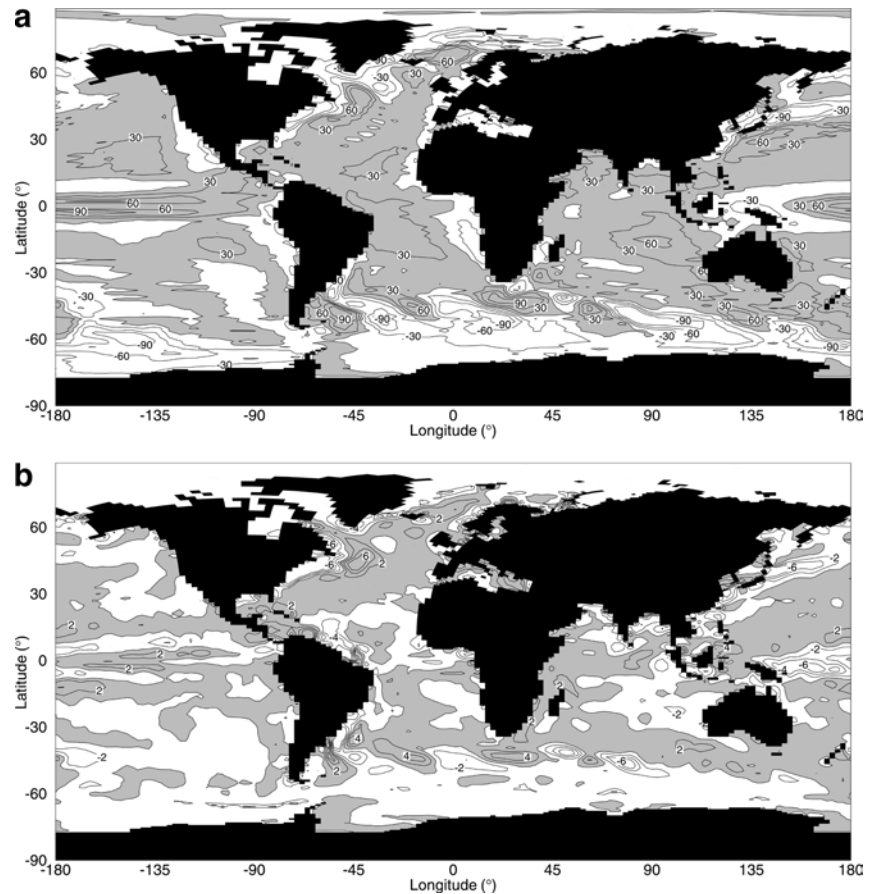
## 4 Experimental design

The ocean model is initialised with January climatological salinity and temperature fields from Levitus et al. (1994) and Levitus and Boyer (1994), respectively. The ocean model is then integrated for 125 years, forced with reanalysed atmospheric surface fields during 1976–1999 from the NCEP/NCAR dataset (Kalnay et al. 1996), using the parameterisation of the surface fluxes as described in Bentsen and Drange (2000). During the spinup, the sea-surface salinity (SSS) and SST fields are relaxed towards monthly mean climatology. The relaxation is carried out by applying fluxes of salt and heat proportional to the SSS and SST differences between model and climatology, respectively. The mismatch between model and climatology is limited to  $|\Delta SSS| < 0.5$  psu and  $|\Delta SST| < 1.5$  °C to avoid extreme relaxation fluxes in the vicinity of the western boundary currents which are not realistically separated from the coasts in the model with the current resolution. The e-folding time scale for the relaxation is 30 days for a mixed layer of 50 m or less, decreasing linearly with increased mixed layer depths.

The atmospheric component uses a standard meteorological analysis for numerical weather forecasts from ECMWF as initial state. The model is then integrated for 10 days with SST, sea-ice and albedo taken from the last 10 days of the spinup of the ocean model. After that the system is run in coupled mode for 10 years with SSS and SST relaxed towards climatology with an e-folding time scale of 10 days. Another 10 years are integrated with a weaker relaxation (the e-folding time scale is increased to 30 days), and for this period the corresponding relaxation fluxes are stored to produce average restoring terms (flux adjustments). These fluxes are divided into 48 time intervals annually, so the annual cycle of the averaged fluxes are captured. The annual mean diagnosed fluxes of heat and salt are shown in Fig. 2.

Despite generally small flux values, there are some areas of large fluxes of both salt and heat, especially in the vicinity of the western boundary currents. Salt and heat are added in the Greenland and the Norwegian seas, indicating that the transport of Atlantic water into the Nordic Seas is too weak. Large fluxes of salt and heat go into the equatorial Pacific, which is caused by a too strong upwelling of cold and freshwater masses in that region. Also, the flux adjustments remove heat from the Southern Ocean.

**Fig. 2** Annual mean surface flux adjustments of **a** heat and **b** salt. The contour interval is  $30 \text{ Wm}^{-2}$  and  $2 \cdot 10^{-6} \text{ (kg salt) m}^{-2} \text{ s}^{-1}$  for heat and salt fluxes, respectively. Positive values are shaded



For the remaining 300 years of the coupled integration, the fluxes computed by the atmosphere model and given to the ocean model, are adjusted by adding the diagnosed restoring fluxes. This 300-years period has formed the basis for the comparison between model and observations or reanalysis data shown in the next two sections.

## 5 Model performance

### 5.1 Model stability

The time evolution of the global mean SST is shown in Fig. 3a. The SST shows a realistic mean state and seasonal cycle. However, there is a non-uniform trend towards higher temperatures, with a net increase of approximately  $0.3 \text{ }^\circ\text{C}$  over 300 years. The drift may indicate that the time period used to calculate the flux adjustment was too short. As the flux adjustment was calculated over only 10 years, interdecadal variability in the model may have led to inaccurate flux adjustment terms. Another possibility is that the drift is due to feedback from long term changes in the deeper ocean.

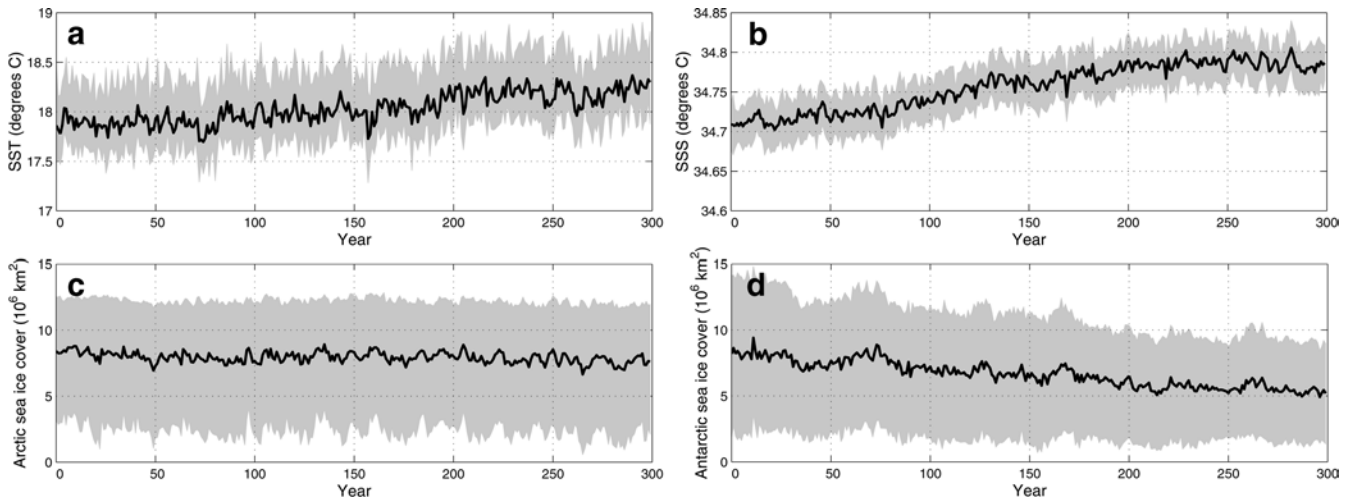
For SSS there is a drift towards higher global mean values during the first 200 years, while there is practically no trend during the remaining 100 years of the integration. The overall drift is near  $0.02 \text{ psu}$  per century.

The total sea-ice area in the Arctic is close to climatology both for the annual mean and the seasonal cycle,

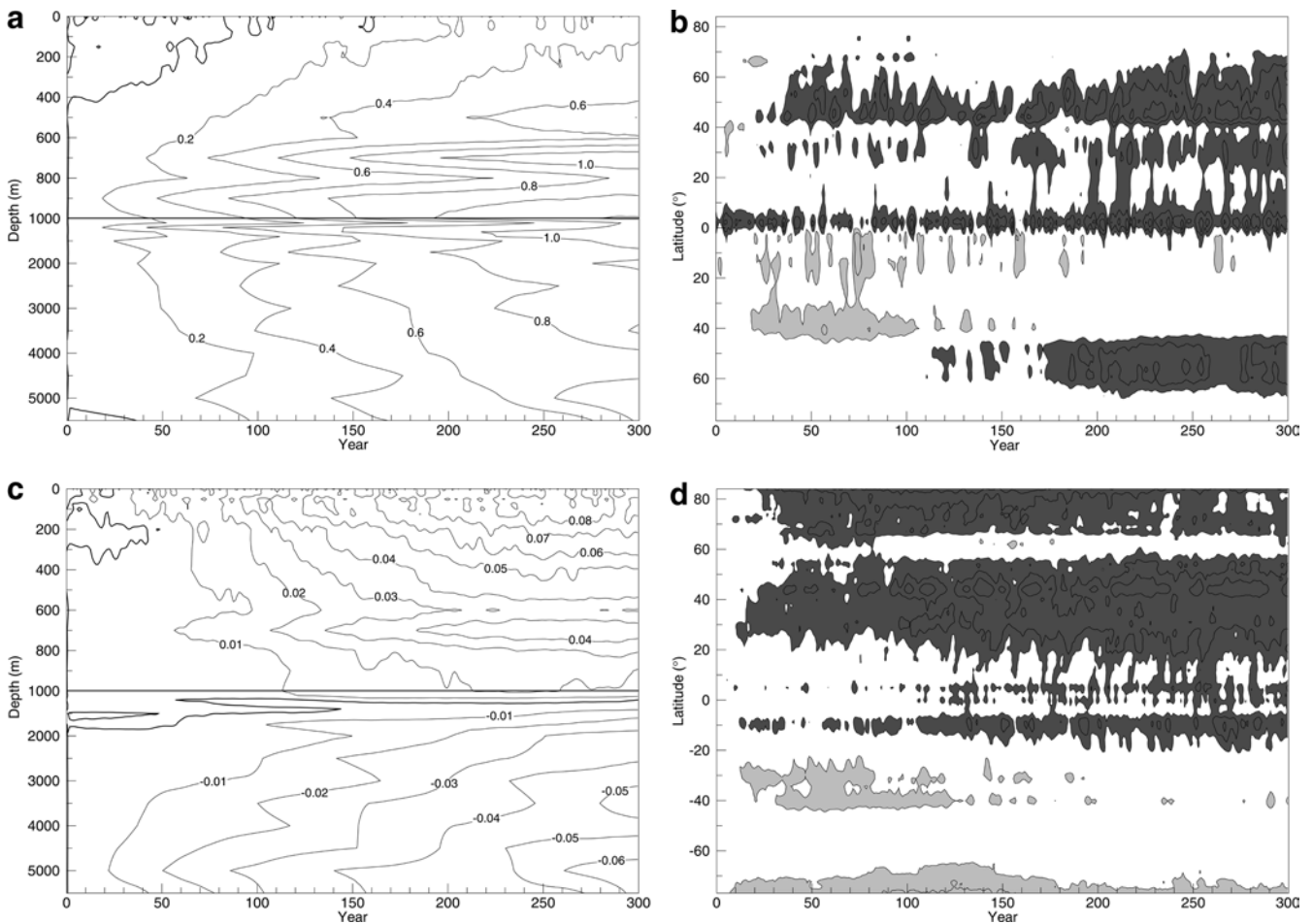
with a weak drift towards slightly less sea-ice cover (Fig. 3c). For Antarctica, there is a reduction in the sea-ice cover during the first 200 years of the integration, while the sea-ice cover is fairly stable in the remaining part of the integration. As shown in Fig. 3d, the decrease in the annual mean is mainly reflecting the changes in the winter extent of the ice. During summer, there are no significant changes in the sea-ice extent.

Figure 4a shows the ocean temperature drift as a function of time and depth. There is a significant positive temperature drift in the deep ocean, while near the surface, where the flux adjustment is efficient, the drift is small. The annual global mean net flux adjustment of heat is  $5.0 \text{ Wm}^{-2}$  (positive into the ocean). During 300 years this flux alone will heat up a 4000 m deep ocean column by almost  $3 \text{ }^\circ\text{C}$ , and this imbalance in the flux adjustments is believed to be the main reason for the warming of the deep ocean. The heat is added to the deep ocean through convective mixing at high latitudes and gradually spreads by the thermohaline circulation. The SST difference, described as a function of time and latitude in Fig. 4b, shows a warming trend between  $40$  and  $60^\circ\text{N}$ . The equatorial region has a slight warming trend and a large variability on an interannual time scale. A warming can also be seen south of  $40^\circ\text{S}$ .

In Fig. 4c, the salinity drift as a function of time and depth is shown. Below 1000 m, the ocean becomes less saline during the integration, while closer to the surface



**Fig. 3** Time series of annual mean global SST **a**, SSS **b**, Arctic **c** and Antarctic **d** sea-ice cover. The *shaded regions* represent the spread of the daily mean data



**Fig. 4** **a, b** Temperature and salinity **c, d** differences relative to the start of the integration. *Left panels* show the globally averaged differences with contour intervals of 0.1 °C **a** and 0.01 psu **c**. *Right panels* show the zonally averaged surface differences with contour

intervals 0.3 °C **b** and 0.1 psu **d**. Here *light shaded areas* are below respectively  $-0.3\text{ °C}$  and  $-0.1\text{ psu}$ , while the *dark shaded areas* are above 0.3 °C and 0.1 psu

there is a positive salinity trend. As for heat, there is an imbalance in the flux adjustment of salt which is believed to cause the deep ocean to freshen. The annual global

mean net salt flux adjustment is  $-0.5 \cdot 10^{-7}\text{ kg m}^{-2}\text{ s}^{-1}$  (corresponds to adding  $0.1\text{ mm day}^{-1}$  of freshwater), which during the 300-year integration will change the

mean salinity of a 4000 m deep ocean column by almost  $-0.12$  psu. Most of the freshening of the deep ocean occurs in the Southern Hemisphere. The SSS difference as a function of time and latitude (Fig. 4d), indicate a positive salinity trend in the Northern Hemisphere, while the zonal SSS in the Southern Hemisphere remains fairly constant during the integration.

Table 3 summarises the global annual averages of key atmospheric and surface variables in the simulation and reported values from the literature. In addition the trends and Spearman rank correlations are given. The Spearman rank correlation is a measure of any monotonic trend (not necessarily linear) in the time series. Values close to  $\pm 1$  indicate a significant trend.

Both globally averaged annual, DJF and JJA surface air temperatures (T2m) are close to the values of the NCEP reanalysis (Table 3). There is an average global warming trend of  $0.18$  °C per century. This seems to be associated with a decrease in the Antarctic sea-ice extent throughout the simulation, which contributes both locally, and through the influence on the equator to pole gradient in temperature and the corresponding changes in the heat transport.

The slight warming is affecting the amount of precipitable water which increases with  $0.2$  kg m<sup>-2</sup> (0.9%) per century due to the ability of the warmer atmosphere to

keep more water vapour. This in turn affects the downward longwave radiation which increases with  $0.9$  Wm<sup>-2</sup> (0.3%) per century and the latent heat flux which decreases with  $0.4$  Wm<sup>-2</sup> (0.4%) per century due to the smaller specific humidity gradients near the surface.

## 5.2 Global energy budgets, cloud cover and cloud forcing

Compared to ISCCP D2 data (Rossow and Schiffer 1991; Rossow and Zhang 1995), the model simulates annual globally averaged total cloud cover well, with a value of 67.9% compared to 67.7% for the ISCCP D2 dataset (Table 3). In addition, both annual and monthly zonal averages agree well (Fig. 5) with monthly biases being less than 15% at all latitudes except for the polar areas during summer, where the model overestimates the Arctic cloud cover with 25% in September. The overestimation of Arctic cloud cover is a feature seen in many GCMs through the reason for the overestimation is not fully understood (Beesley and Moritz 1999). The model has a small prevailing underestimation of cloud cover in the subtropical regions that is associated with the positioning of the Hadley cell (see Fig. 9). There is

**Table 3** Global area weighted averages, linear trends and Spearman rank correlations for variables over the 300-year integration

Variable	Average			Trend (100 yrs <sup>-1</sup> )	Spearman correlation
	BCM	OBS	Unit		
SST	18.03	18.15 <sup>a</sup>	°C	0.142	0.81
SSS	34.76	34.64 <sup>b</sup>	psu	0.031	0.93
Arctic sea ice	7.93	10.72 <sup>c</sup>	10 <sup>6</sup> km <sup>2</sup>	-0.158	-0.33
Antarctic sea ice	6.64	10.21 <sup>c</sup>	10 <sup>6</sup> km <sup>2</sup>	-1.024	-0.91
2 m ANN temperature	14.19	13.76 <sup>d</sup>	°C	0.175	0.81
2 m DJF temperature	12.39	12.29 <sup>d</sup>	°C	0.163	0.62
2 m JJA temperature	15.96	15.34 <sup>d</sup>	°C	0.188	0.85
Cloud cover	67.84	67.65 <sup>e</sup>	%	-0.026	-0.09
Precipitation	3.10	3.05 <sup>e</sup>	mm day <sup>-1</sup>	0.014	0.68
Precipitable water	24.70	23.99 <sup>f</sup>	kg m <sup>-2</sup>	0.218	0.64
Runoff (land)	0.74	0.73 <sup>g</sup>	mm day <sup>-1</sup>	0.005	0.15
TOA net longwave radiation	-235.11	-235 <sup>h</sup>	Wm <sup>-2</sup>	-0.260	-0.53
TOA net clear sky longwave radiation	-267.08	-265 <sup>h</sup>	Wm <sup>-2</sup>	-0.359	-0.75
TOA net shortwave radiation	234.98	235 <sup>h</sup>	Wm <sup>-2</sup>	0.223	0.42
TOA net clear sky shortwave radiation	290.68	285 <sup>h</sup>	Wm <sup>-2</sup>	0.265	0.89
TOA net cloud radiative forcing	-23.73	-20 <sup>h</sup>	Wm <sup>-2</sup>	0.057	0.13
TOA net longwave cloud radiative forcing	31.97	30 <sup>h</sup>	Wm <sup>-2</sup>	0.099	0.51
TOA net shortwave cloud radiative forcing	-55.70	-50 <sup>h</sup>	Wm <sup>-2</sup>	-0.042	-0.10
Surface net radiation	103.69	102 <sup>h</sup>	Wm <sup>-2</sup>	0.240	0.48
Surface net longwave radiation	-49.33	-66 <sup>h</sup>	Wm <sup>-2</sup>	0.064	0.28
Surface downward longwave radiation	332.38	324 <sup>h</sup>	Wm <sup>-2</sup>	0.886	0.76
Surface net shortwave radiation	153.01	168 <sup>h</sup>	Wm <sup>-2</sup>	0.175	0.32
Surface downward shortwave radiation	175.99	198 <sup>h</sup>	Wm <sup>-2</sup>	-0.054	-0.11
Sensible heat flux	-17.86	-24 <sup>h</sup>	Wm <sup>-2</sup>	0.089	0.47
Latent heat flux	-87.60	-78 <sup>h</sup>	Wm <sup>-2</sup>	-0.377	-0.66

Values close to 1 or  $-1$  of the Spearman rank correlation indicates a significant monotonic trend (not necessarily linear) in the time series

<sup>a</sup>Reynolds and Smith (1994)

<sup>b</sup>Levitus et al. (1994)

<sup>c</sup>Satellite data 1978–1995 interpolated to model grid (Björge et al. 1997)

<sup>d</sup>NCEP reanalysis 1950–1990 (Kalnay et al. 1996)

<sup>e</sup>ISCCP D2 1984–1993 (Rossow and Schiffer 1991; Rossow and Zhang 1995)

<sup>f</sup>CMAP 1979–1999 (Xie and Arkin 1997)

<sup>g</sup>Baumgartner and Reichel (1975)

<sup>h</sup>Kiehl and Trenberth (1997)

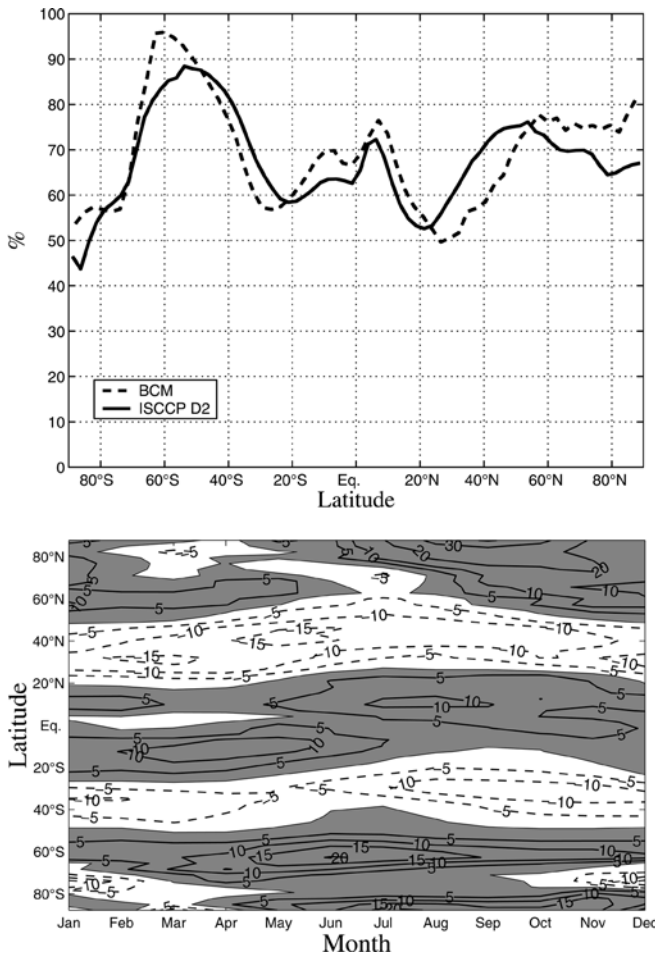


**Fig. 5** Zonal average of **a** annual total cloud cover and **b** monthly differences between BCM and ISCCP D2 data (BCM-ISCCP). The ISCCP D2 data set is from January 1984 to December 1993. Values are in parts per hundred (%)

also an overestimation of the cloud cover in relation to the underestimation of the Antarctic sea ice in JJA (Fig. 5).

Global averages of net top-of-atmosphere (TOA) longwave and shortwave radiation (Table 3) are well simulated with values of  $-235.1 \text{ Wm}^{-2}$  and  $235.0 \text{ Wm}^{-2}$  respectively, which are well within the error estimates of the satellite observed values (Rieland and Raschke 1999).

The simulated net cloud radiative forcing is  $-23.7 \text{ Wm}^{-2}$  (Table 3) which is within the range of the ERBE and NIMBUS-7 estimates of  $-19 \text{ Wm}^{-2}$  to  $-27 \text{ Wm}^{-2}$ , respectively (Kiehl et al. 1994; Ardanuy et al. 1991). The model thus simulates realistically the different parts of the TOA energy budget and its monthly variations.

The global longwave cloud forcing is estimated to  $32 \text{ Wm}^{-2}$  which is close to the ERBE estimate of  $30 \text{ Wm}^{-2}$  reported by Kiehl et al. (1994). The meridional distribution of the TOA net outgoing longwave radiation (OLR) is also realistically simulated compared to the ERBE data (Harrison et al. 1990; Barkstrom 1984) with deviations of monthly zonal averages from the

ERBE data not exceeding  $15 \text{ Wm}^{-2}$  at any latitude (Fig. 6). The largest difference compared to the ERBE data is in the Southern Hemisphere mid-latitudes during JJA. This is associated with too much cloudiness and the net longwave cloud radiative forcing is  $5\text{--}10 \text{ Wm}^{-2}$  too strong in this region. In the tropics, OLR is too high in DJF and MAM, though the cloud cover and net longwave cloud radiative forcing are well simulated in this region. In the Arctic winter the OLR is too high due to too large cloud amounts absorbing the LW radiation from the colder surface and re-emitting at higher temperatures.

Simulated global TOA average shortwave cloud forcing is  $6 \text{ Wm}^{-2}$  higher than the estimates of Kiehl and Trenberth (1997) (Table 3). Figure 7 shows that in the tropics too much of the shortwave radiation is reflected back to space with errors in monthly zonal means reaching  $30 \text{ Wm}^{-2}$ . The net shortwave cloud radiative forcing is too strong compared to the ERBE data. From Figs. 7 and 9 it is seen that the largest errors are related to the rising branch of the Hadley cell with an overestimation of cloud radiative forcing over all the major ocean areas in this region.

In the marginal ice zones, zonal net monthly mean shortwave radiation reaches  $40 \text{ Wm}^{-2}$  too high in the summer months. This is due to a too low sea-ice extent during summer, resulting in a too low albedo.

The net surface shortwave radiation is estimated to be  $153 \text{ Wm}^{-2}$  compared to the  $168 \text{ Wm}^{-2}$  estimate of Kiehl and Trenberth (1997) (Table 3). However, most estimates of surface radiation are based on satellite TOA measurements as input to radiation models. Observational studies indicate that current radiative models may underestimate the clouds ability to absorb shortwave radiation (e.g., Ramanathan et al. 1995). Thus global estimates range from  $142 \text{ Wm}^{-2}$  (Ohmura and Gilgen 1993, observational based) to  $174 \text{ Wm}^{-2}$  (Paltridge and Platt 1976). We therefore conclude that the simulated net surface shortwave radiation probably is underestimated, although within current estimates. Comparisons of monthly zonal averages of surface radiation terms with the satellite based estimates from the Surface Radiation Budget (Whitlock et al. 1995; Darnell et al. 1992) data (not shown) revealed much the same patterns as the ERBE TOA comparisons.

### 5.3 Precipitation and net freshwater flux

Global annual average precipitation (Table 3) is close to climatological estimates with  $3.10 \text{ mm day}^{-1}$  compared to  $3.05 \text{ mm day}^{-1}$  from the CMAP data (Xie and Arkin 1997). Precipitation is a difficult field to observe and the zonal mean climatologies may differ by as much as 40% in the tropics, but in general the model zonal mean distribution (Fig. 8) shows the same pattern as the observations. However the amplitude of the second maximum in the South Pacific (the South Pacific Convergence Zone) seems to be too high and situated

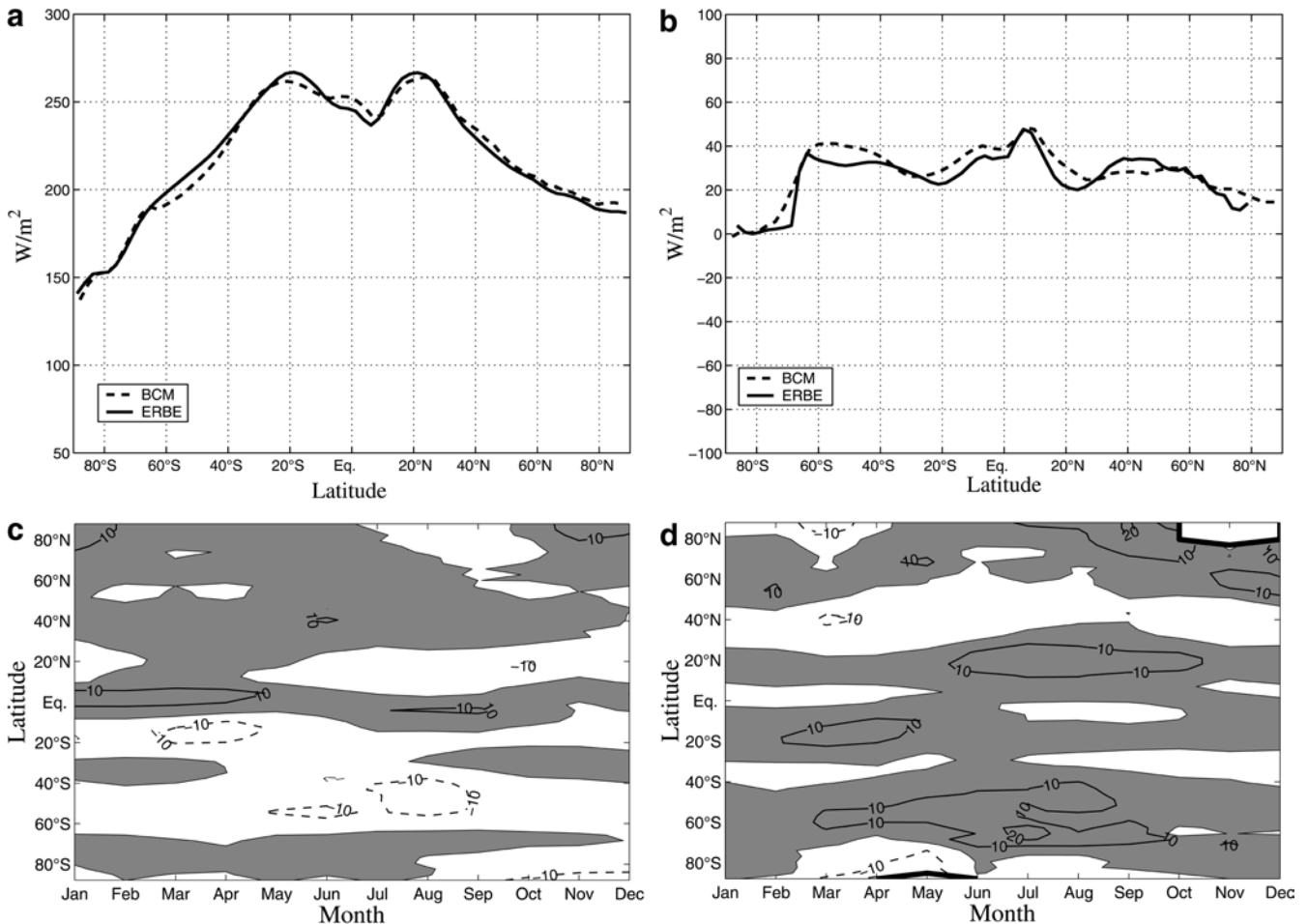


**Fig. 6** Zonal average of **a** annual TOA net longwave radiation and **b** net longwave cloud forcing. Monthly differences between BCM and ERBE data (BCM-ERBE) **c** of TOA net longwave radiation

and **d** net longwave cloud forcing. The ERBE data is from February 1985 to May 1989. Units are in  $\text{Wm}^{-2}$

too far south, a feature shared with many other AOGCMs (Covey et al. 2000). Monthly differences between the BCM simulation and the climatological datasets show that the largest differences in the tropics are related to the MAM season where the model underestimates the precipitation both compared to the CMAP (Xie and Arkin 1997) and the GPCP (Huffman et al. 1995) climatologies. There is also an incorrect location and possibly an overestimation of the precipitation maximum in JJA related to the simulated width and the strength of the rising branch of the Hadley cell. Net freshwater fluxes over the ocean are compared to estimated values of da Silva et al. (1994) and Oberhuber (1988). Both datasets are based on the Comprehensive Ocean–Atmosphere Data Set (COADS) (Woodruff et al. 1987). Evaporation is estimated using bulk formulas in both cases. In the da Silva dataset the precipitation is derived from Present Weather (PW) information of standard ship reports (Tucker 1961; Dorman and Bourke 1978), while the Oberhuber dataset is based on land and island station records complemented by satellite observations (Shea 1986). As seen from Fig. 8, the climatological estimates diverge polewards of  $60^\circ\text{N/S}$ .

This is mainly due to the rather unrealistic precipitation estimates in the da Silva dataset, which differs significantly from other precipitation climatologies in these regions. The simulated average zonal patterns in the net freshwater flux agrees well with the climatologies, but there seems to be too much evaporation in the Southern Hemisphere high-pressure belt. This is related to too strong subsidence in this area (see Fig. 9) and an underestimation of the cloud cover. The monthly mean differences in freshwater fluxes between the Oberhuber climatology and the simulations (Fig. 8) reveal to a large extent the same pattern as the precipitation comparison. In MAM, the underestimation of precipitation in the equatorial belt leads to an underestimation in the freshwater flux here. The overestimation of tropical precipitation in JJA is associated with the model's representation of the rising branch of the Hadley cell.

#### 5.4 Atmospheric mean circulation

The simulation reproduces the annually averaged meridional circulation with fairly realistic positions and

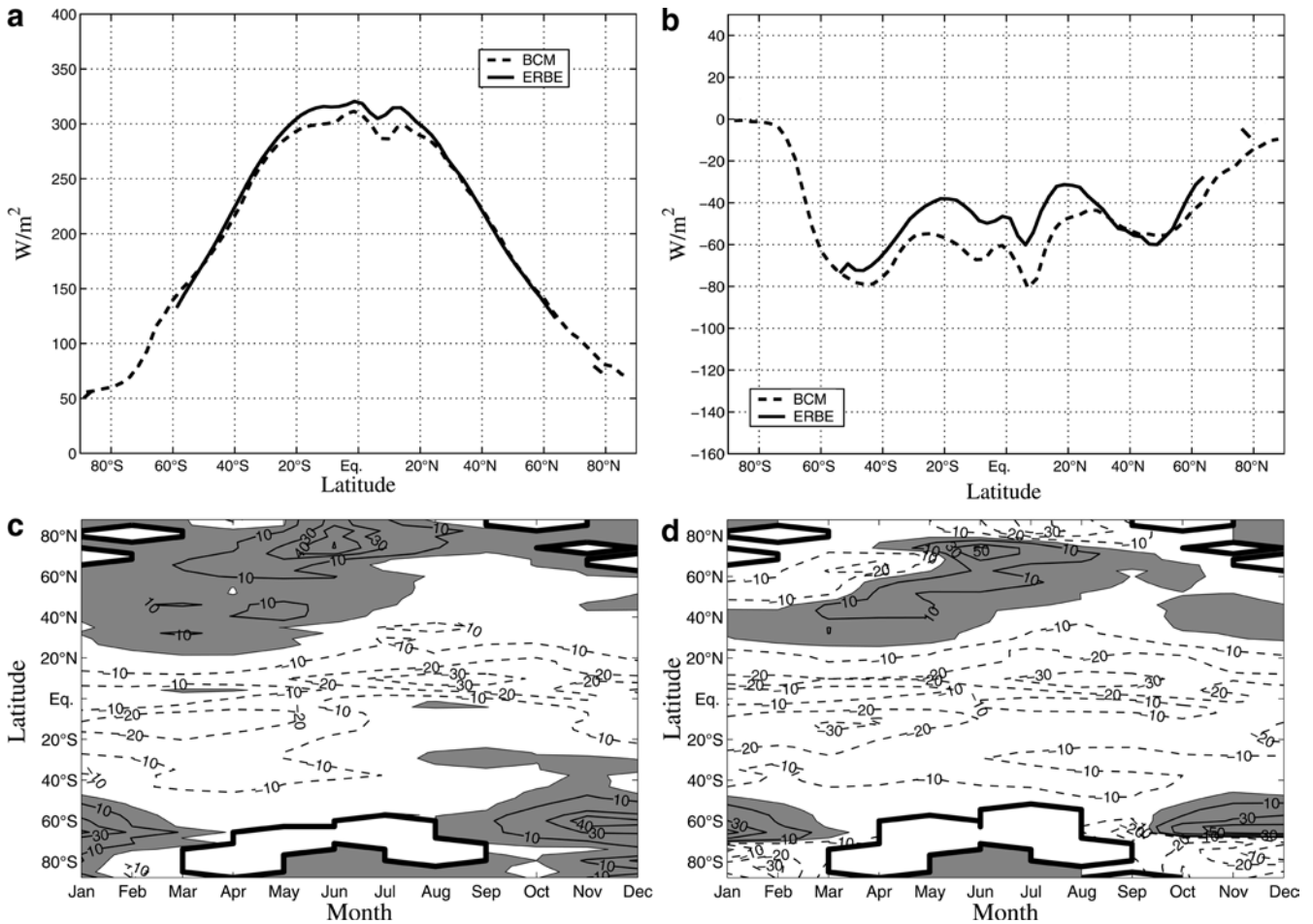


**Fig. 7** Zonal average of **a** annual TOA net shortwave radiation and **b** net shortwave cloud forcing. Monthly differences between BCM and ERBE data (BCM-ERBE) **c** of TOA net shortwave

radiation and **d** net shortwave cloud forcing. The *tick line* marks the areas where there are no observational data. The ERBE data is from February 1985 to May 1989. Units are in  $\text{Wm}^{-2}$

values of both the Hadley, the Ferrel and the polar cells. The Hadley cells are however slightly broader than in the reanalysis and the annual mean strength is overestimated by  $\sim 10\text{--}30\%$  compared to the NCEP estimates. The overestimation is most pronounced in JJA. From Fig. 9 it can be seen that in DJF the core of the Hadley cell is too far south. The maximum in the mass stream function at  $\sim 300$  hPa is approximately  $20 \cdot 10^{10} \text{ kg s}^{-1}$  at  $5^\circ\text{N}$  compared to  $15 \cdot 10^{10} \text{ kg s}^{-1}$  at  $10^\circ\text{N}$  in the NCEP reanalysis. The DJF Ferrel cells are well positioned in both hemispheres, but the strength of the cell in the Northern Hemisphere is overestimated. A significant overestimation is seen in the Hadley cell in JJA (Fig. 9), where the maximum of the simulated cell is around  $26 \cdot 10^{10} \text{ kg s}^{-1}$  compared to  $17 \cdot 10^{10} \text{ kg s}^{-1}$  in the NCEP reanalysis. The positioning of the JJA cell is fairly good, but slightly broader than in the reanalysis. Figure 10 shows the positioning and strength of the zonally averaged zonal component of the wind. The positioning and strength of the subtropical jet-streams are well simulated both in DJF and JJA (Fig. 10) with errors in the order of  $2 \text{ ms}^{-1}$ . However there are some errors in the simulation of the lower stratospheric jets. This is related to

substantial errors in the horizontal temperature gradients in the same area (Fig. 11), a feature that may be due to too low vertical resolution in the lower stratosphere.

The general impression of the simulated zonal mean temperature structure is that it is in good agreement with the reanalyses. Both seasonal and spatial variations are well captured. There are however some disagreements. The stratosphere is too cold and the horizontal temperature gradients between the poles and equator are too weak. This is consistent with the weak stratospheric model jets shown in Fig. 10. In the Arctic region we see that the temperature is too high during summer.

The distribution of the mean SLP in the NCEP reanalysis and the model run is illustrated in Fig. 12 for DJF and JJA. In general, the mean SLP is well simulated. In the boreal winter (DJF) the Icelandic and the Aleutian lows are correctly located, but weaker than in the NCEP reanalyses. The Azores high is too extensive and slightly misplaced towards the African coast, and the Siberian high is somewhat too weak. Over the Arctic, the SLP is generally overestimated, except over Greenland where the SLP is too weak compared to NCEP. In the Southern Hemisphere the Antarctic circumpolar

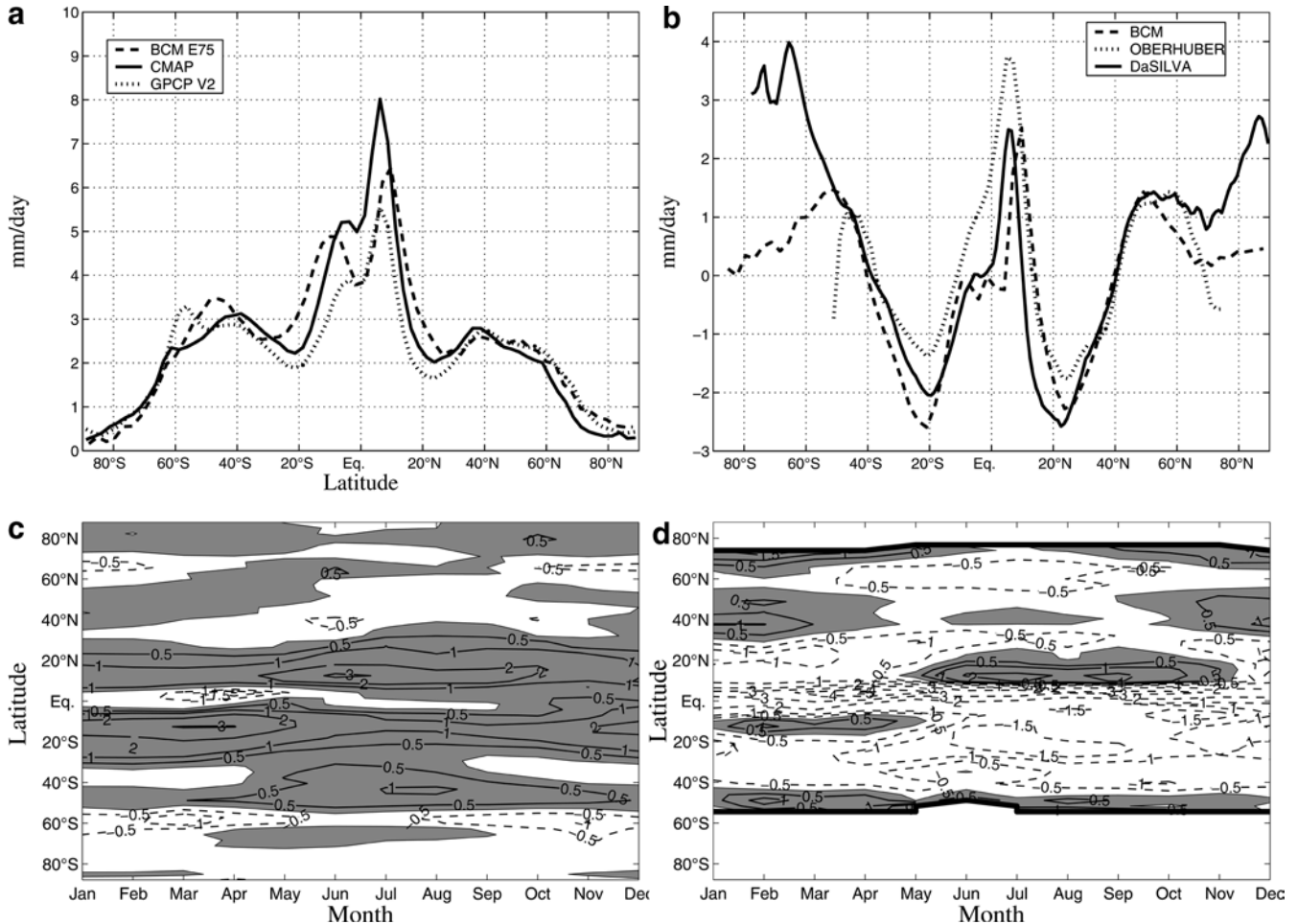


**Fig. 8** Zonal average of **a** annual precipitation, **b** net freshwater flux and monthly differences between BCM and observations (BCM-observations) for **c** precipitation and **d** net freshwater flux. The observations used are GPCP data (Huffman et al. 1995) from

January 1979 to December 2000, and net freshwater estimates based on COADS data (da Silva et al. 1994) January 1945 to December 1989, and Oberhuber (1988) January 1950 to December 1979. Units are in  $\text{mm day}^{-1}$

trough is too weak. However, due to artificial surface pressure trends one may question the correctness of the reanalysed SLP field here (Hines et al. 2000). During JJA, the Northern Hemisphere subtropical highs are well placed, although somewhat too intense. Over the Arctic, the pressure is too high, whereas the pressure is too low over the Antarctic.

In summary, the BCM surface pressure field reveals the same deficiencies and strengths as most other coupled models (Lambert and Boer 2001). Additionally, in common with the second Hadley Centre AOGCM (Johns et al. 1997), Fig. 12 shows that the North Atlantic storm track in the model is too zonal and displaced to the south compared to the storm track in the NCEP reanalysis.

The model's ability to reproduce the interannual variability is relatively good. This is illustrated in Fig. 13 which shows the detrended interannual standard deviation of DJF mean SLP for BCM compared to the NCEP reanalysis data. The modelled standard deviation is similar to the reanalysis in the Northern Hemisphere, although the extent of the maximum low-frequency

variability is smaller over the North Atlantic region in the BCM. In the Pacific, the maximum variability is shifted to the northeast as compared to NCEP. In the tropical regions and in the Southern Hemisphere, the agreement between the simulated and reanalysed variability is also good.

Figure 14 displays the 2 m temperature difference between BCM and Jones (1994) data for DJF and JJA. The simulated temperatures agree rather well with the observations with exceptions for the polar regions. The overestimation of the air temperature in the Arctic during winter is mainly a consequence of too thin sea-ice and a too strong heat flux from the ocean. Similarly, it can be seen that too little Antarctic sea-ice results in large temperature differences in the Weddell Sea during JJA as compared to the observations. Outside the polar regions the temperature deviations from the observations are over land generally on the order of  $\pm 2$  °C. However, in particular in regions of elevated terrain the differences are somewhat larger. Differences in temperatures from observations are generally small over the ocean.

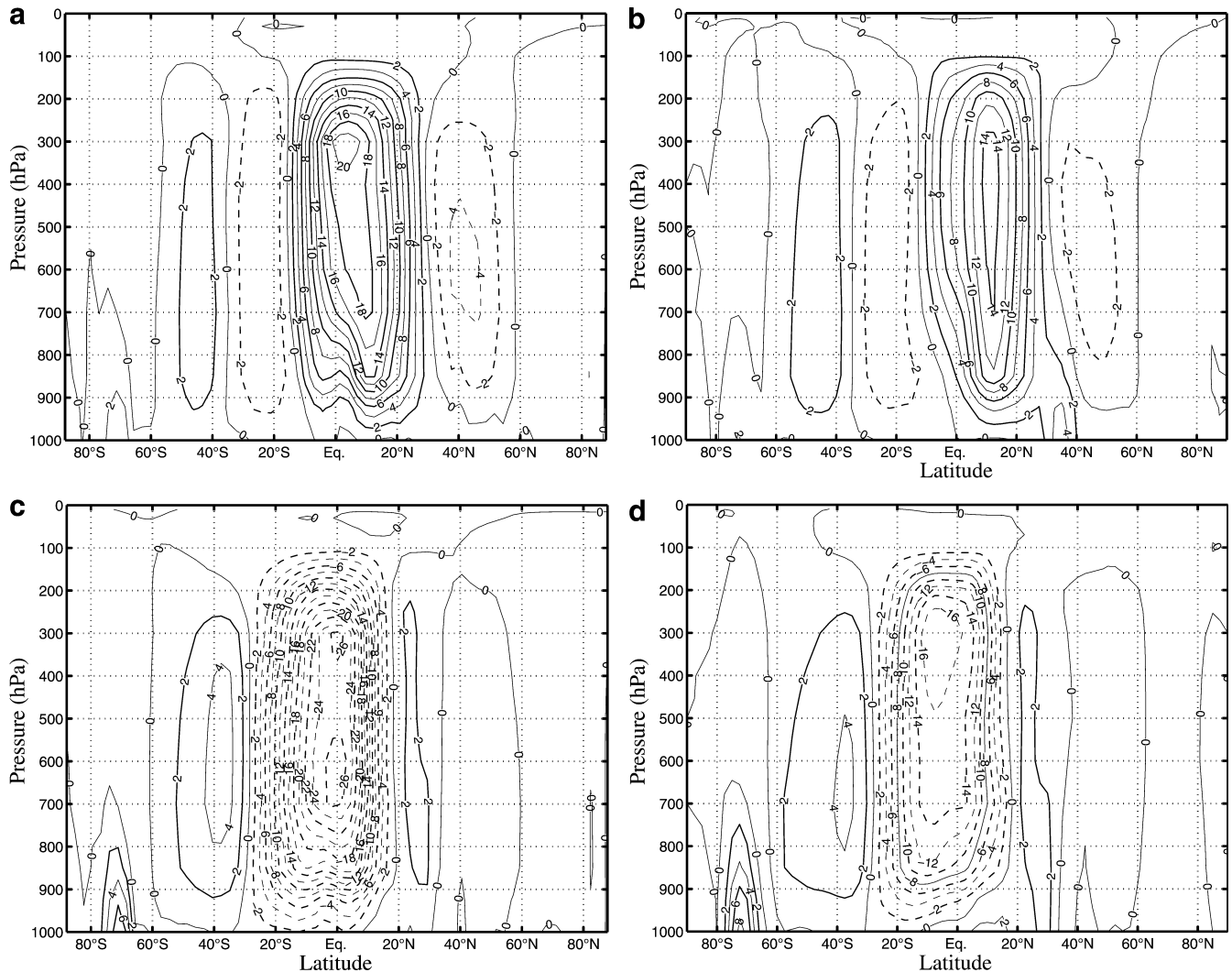


**Fig. 9** DJF (upper) and JJA (lower) zonal-average of mass stream function ( $10^{10} \text{ kg s}^{-1}$ ) in BCM (left) and NCEP (right). Dashed lines indicate negative values and solid positive. NCEP values are averages from January 1950 to December 1989

### 5.5 Upper ocean properties

The difference between the mean simulated (300 years) and climatological SST is shown in Fig. 15a. At low latitudes, the SSTs are generally slightly too low. Some areas north of  $60^\circ\text{N}$  and south of  $50^\circ\text{S}$  are warmer than the climatology, mainly associated with an underestimation of the ice extent in the polar regions. Substantial temperature differences are found in the vicinity of the western boundary currents (Kuroshio and Gulf Stream), which is caused by an unrealistic separation of these currents from the coast. The largest discrepancy from climatology is found in the equatorial Pacific. This region is associated with too strong upwelling in the model. One reason for this is linked to the fact that the ocean model does not, in the present configuration, have enough isopycnic layers to properly represent the light and highly stratified near surface water masses in the equatorial regions. The mixed layer will then communicate rapidly with a relative thick and cold layer

beneath, resulting in upwelling of a too cold water mass. In a previous version of BCM without flux adjustment, the model went into a permanent cold La Niña like circulation, which again suppressed the variability in the area. As will be shown in Sect. 6, this problem is not present now. Along the west coasts of North and South America, and Africa, the surface water masses are found to be too warm, indicating too weak upwelling in the areas, or a systematic negative bias in the cloud cover.

Figure 15b shows the difference between mean simulated and climatological SSS. Too saline surface water is found in Northern Pacific and Indian Ocean. The South Atlantic is too fresh, while in the North Atlantic the subpolar gyre and the area close to the ice edge are too saline. This may partly be due to the Gulf Stream separating from the North American coast too far north. The Arctic is not shown in the figure due to the limited quality of the Levitus data in that region. However, compared to the salinity climatology by Steele et al. (2001), the Arctic is generally too saline with a

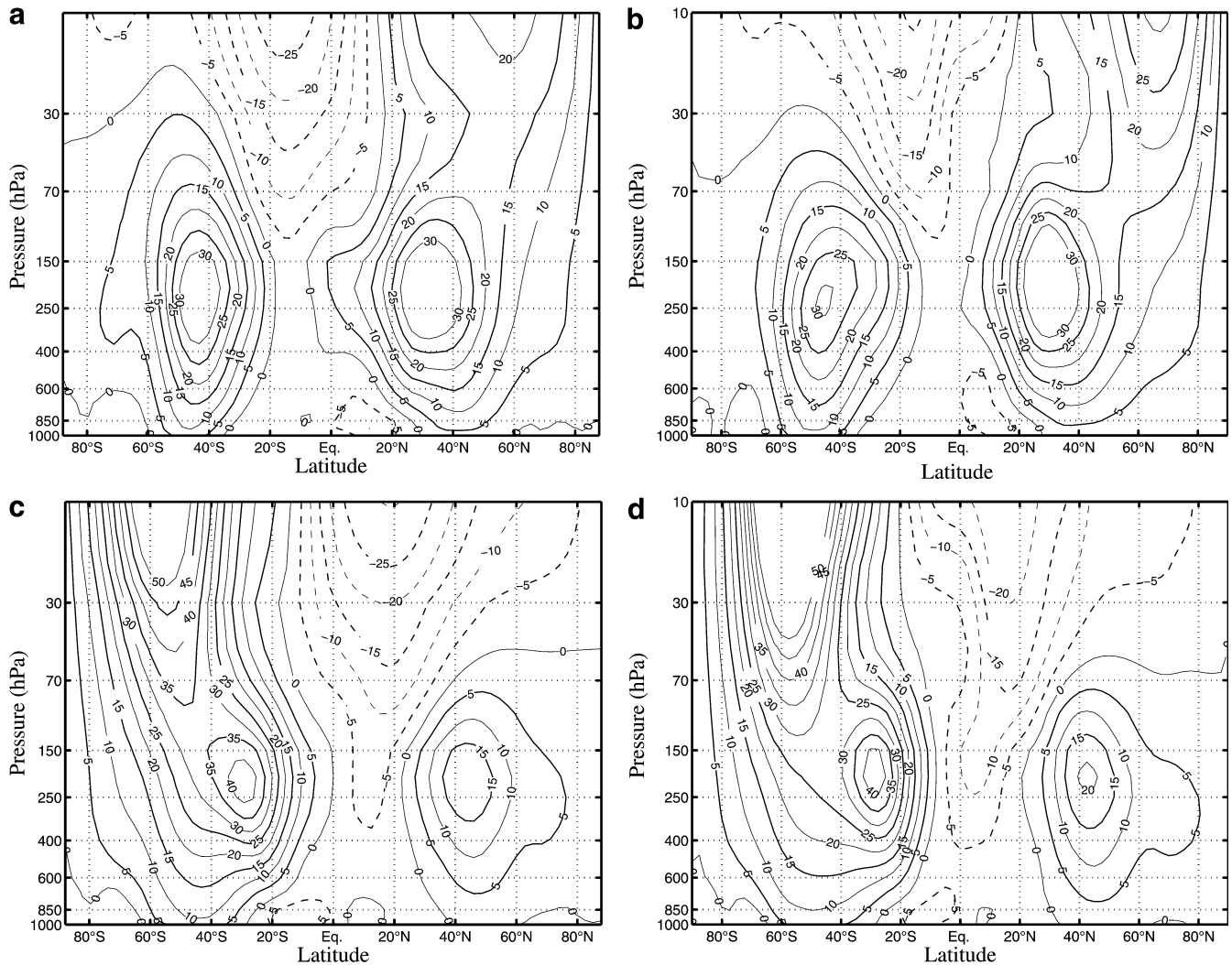


**Fig. 10** DJF (upper) and JJA (lower) zonal-average of zonal wind component ( $\text{ms}^{-1}$ ) in BCM (left) and NCEP (right). Dashed lines indicate easterly values and solid westerly. NCEP values are averages from January 1950 to December 1989

mean mixed layer salinity of  $\sim 33$  psu for most of the region. The largest deviations from the Levitus data are found near many of the tropical river mouths, indicating too little runoff, too deep mixing in the ocean model, or simply that the Levitus data are inaccurate in these regions.

The pattern of the SST differences is in fairly good agreement with the annual mean heat flux adjustments shown in Fig. 2a, while the pattern of SSS differences in most of the Northern Hemisphere does not match well with the annual mean salt adjustment in Fig. 2b. This can be attributed to the difference in the ocean response time for atmospheric heat and freshwater flux anomalies, with a more direct adjustment of SST than of SSS.

The mean sea-ice thickness for the 300-year integration is shown in Fig. 16. The main features of simulated Arctic March ice extent and thickness (Fig. 16a) are well captured as compared to the observations (Bjørge et al. 1997; Parkinson et al. 1999; Bourke and McLaren 1992). However, the ice thickness is generally

too thin and in most areas only 50% of what observations indicate (Rothrock et al. 1999). In September, the Arctic ice extent is generally too small if the area inside the 0.1 m contour is considered to define the region where ice is most likely to be found this month (Fig. 16b). The atmospheric conditions for freezing during the winter seems to be realistically simulated, since the ice extent in winter is in good agreement with observations.

In the Southern Ocean, the ice extent is underestimated both for March and September (Fig. 16c, d), and the extent has also a negative trend during the integration (Fig. 3d). The trend of subsurface waters to warm and freshen during the integration as described in Sect. 5.1, reduces the stratification of the water masses in the Southern Ocean, and leads to a gradual deepening of the upper ocean mixed layer. This reduces the ice formation rate as the entrained water masses have a temperature above the freezing temperature, and since the volume of water that needs to be cooled to the freezing point increases.

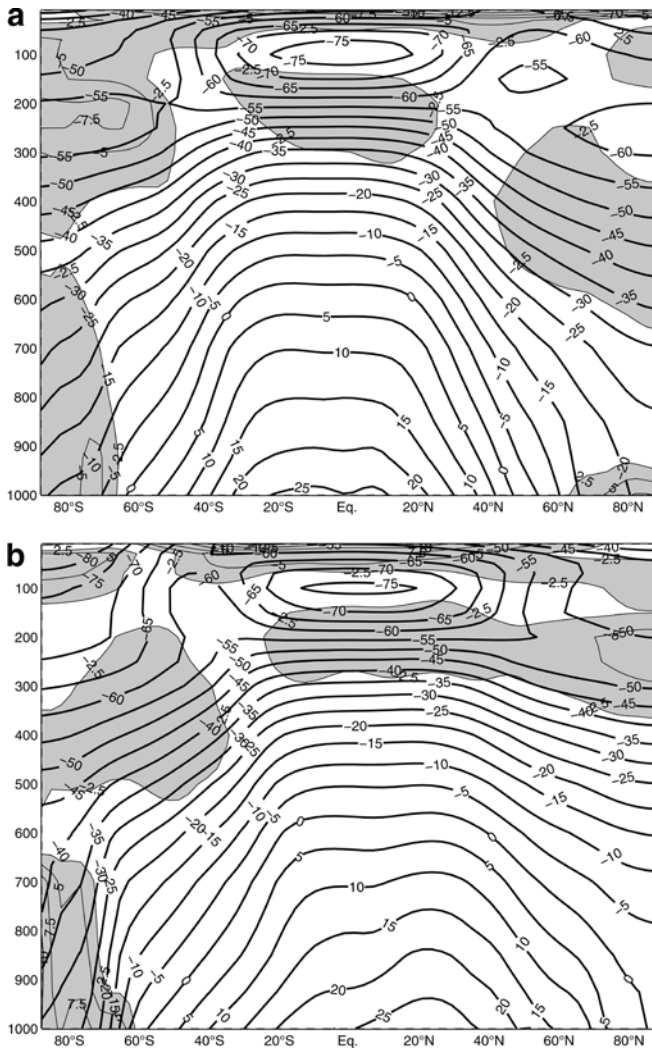


**Fig. 11** a DJF and b JJA zonal-average air temperature ( $^{\circ}\text{C}$ ) in BCM (solid lines) and the difference (dashed lines) between the BCM and NCEP data. Negative values indicate that BCM is colder than the reanalysis. Areas where the temperature differences are larger than  $\pm 2.5^{\circ}\text{C}$  are shaded. NCEP values are averages over the period 1950 to 1989

## 5.6 Ocean mean circulation

The time mean Atlantic meridional overturning stream function has a maximum strength of 18 Sv located at  $25^{\circ}\text{N}$  (Fig. 17). This maximum equals the canonical value, and is in the range of the 15 coupled models studied in Lambert and Boer (2001), where average maximum overturning was 21.1 Sv with a standard deviation of 9.1 Sv. The structure of the overturning is similar to that of the isopycnic model in the model intercomparison by the DYNAMO group (Barnard et al. 1997). A deep negative circulation cell should be present near the bottom, consisting of Antarctic Bottom Water. Because of the choice of reference pressure at the surface when computing potential density, the model is not able to correctly represent the cold, deep waters from the Antarctic. A negative overturning value of 1 Sv near the

bottom matches the mean volume transport through the Bering Strait.

Figure 18 shows the stream function of the vertically integrated mass transport. The major current structures are realistically simulated. The strength of the subtropical gyres in North Atlantic and North Pacific are 30 Sv and 50 Sv, respectively. The strength of the Antarctic Circumpolar Current is indicated by a mean mass transport of 90 Sv through the Drake Passage. In Lambert and Boer (2001), they find an average mass transport through the Drake Passage of 91.9 Sv among the coupled models studied, with a standard deviation of 62.3 Sv. The observational estimates are between 130–140 Sv (Read and Pollard 1993).

## 6 Large-scale variability

Interannual variability has been investigated in terms of the two strongest natural modes of variability of the global climate; the El Niño-Southern Oscillation (ENSO) and the North Atlantic/Arctic Oscillation (NAO/AO). Both of these modes of variability can be detected in a wide range of variables. The focus of this analysis will be on the SLP and the 2 m air temperature (T2m) fields.

### 6.1 The ENSO mode

The atmospheric part of the ENSO, the Southern Oscillation, shows up as the leading mode of variability when a standard empirical orthogonal function (EOF) analysis is performed on the SLP data. In Fig. 19 the EOFs are calculated using the area weighted monthly mean SLP anomalies in the region between  $30^{\circ}\text{S}$  and  $30^{\circ}\text{N}$ . The correlation pattern in BCM shows a dipole structure across the Pacific, where positive pressure anomalies over the western Pacific and the Indian Ocean are associated with negative pressure anomalies spanning a large range of latitudes in the eastern Pacific, having an extension into the North Atlantic. Along the Antarctic continent, there are negative pressure anomalies south of New Zealand and in the Weddell Sea, and a positive anomaly in the southeastern Pacific.

The BCM simulates a realistic pressure pattern compared to the NCEP reanalysis data (Kalnay et al. 1996), where the leading mode of variability shows a similar geographical distribution (Fig. 19b). However, a significant discrepancy is found in the tropical Atlantic, where the NCEP data show anomalies in phase with the western Pacific and Indian Ocean, whereas BCM has almost no correlation there. In the eastern Pacific, the BCM mode shows too strong impact in the equatorial region, and too small impact in the subtropics. From  $30^{\circ}\text{S}$  to  $30^{\circ}\text{N}$ , the leading mode accounts for 17% and 18% of the variability in the BCM and NCEP data respectively. The same analysis has also been performed on the optimal interpolated SLP from the Comprehen-

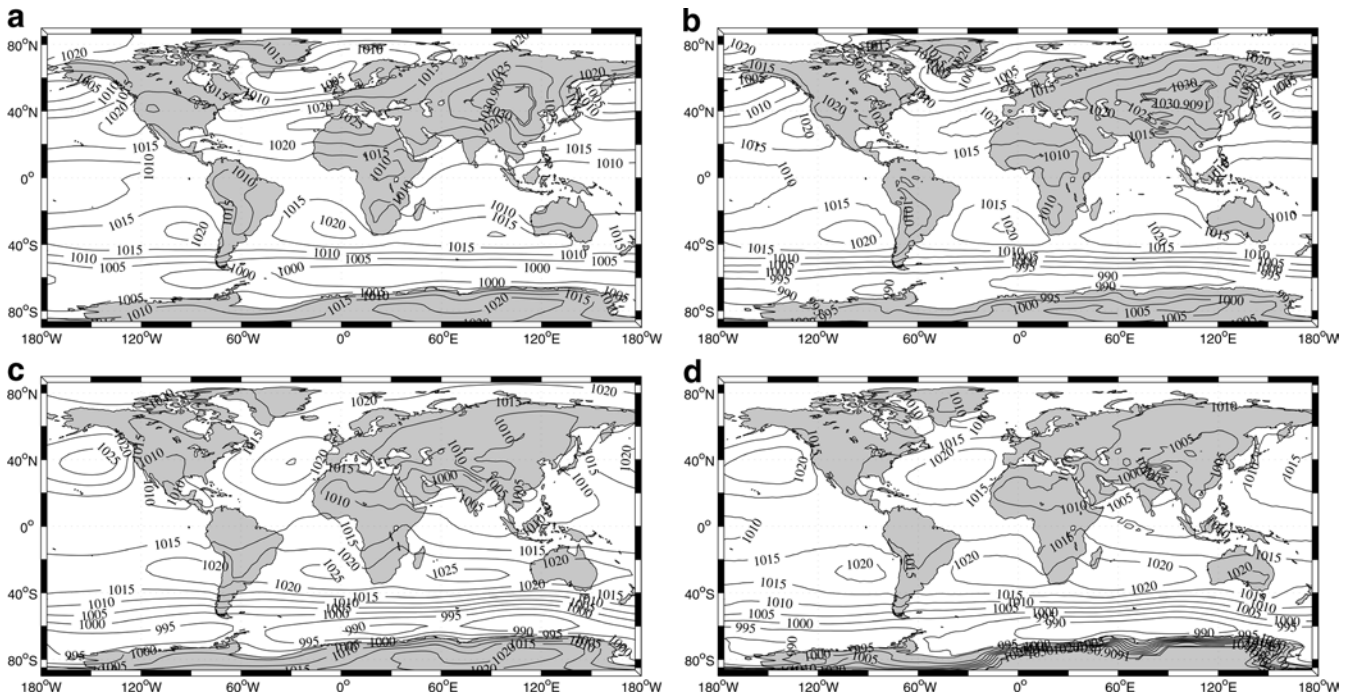


**Fig. 12** Mean sea level pressure (hPa) for BCM (left) and NCEP (right) for winter (upper) and summer (lower) months. NCEP values are averages from January 1950 to December 1989

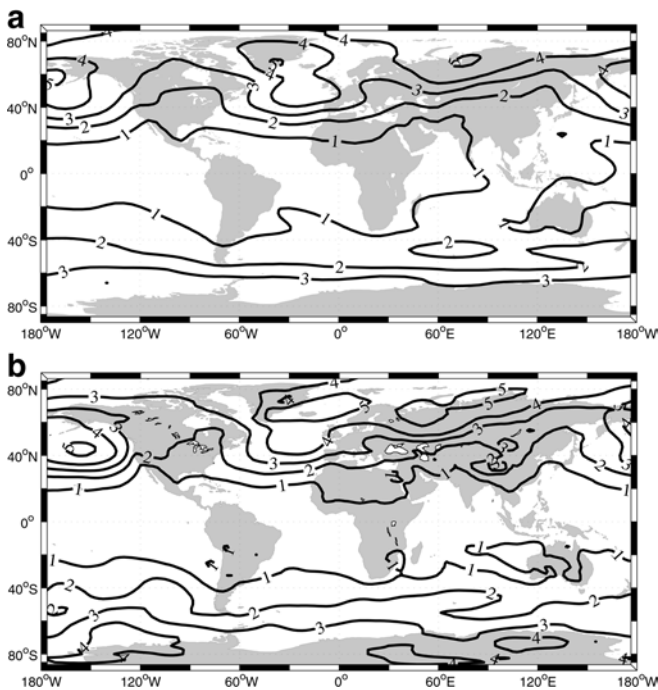


**Fig. 13** Interannual detrended standard deviation (hPa) of DJF sea level pressure for **a** BCM and **b** NCEP. NCEP values are averages from January 1950 to December 1989

sive Ocean–Atmosphere Data Set (COADS) extending back to 1856 (Kaplan et al. 2000), giving a similar pattern as the NCEP data (not shown) but with 20% of the variance explained.

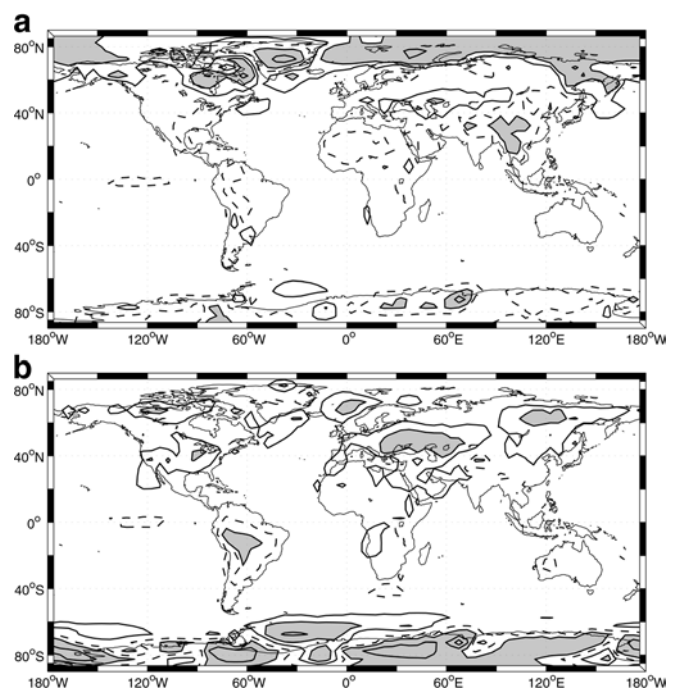
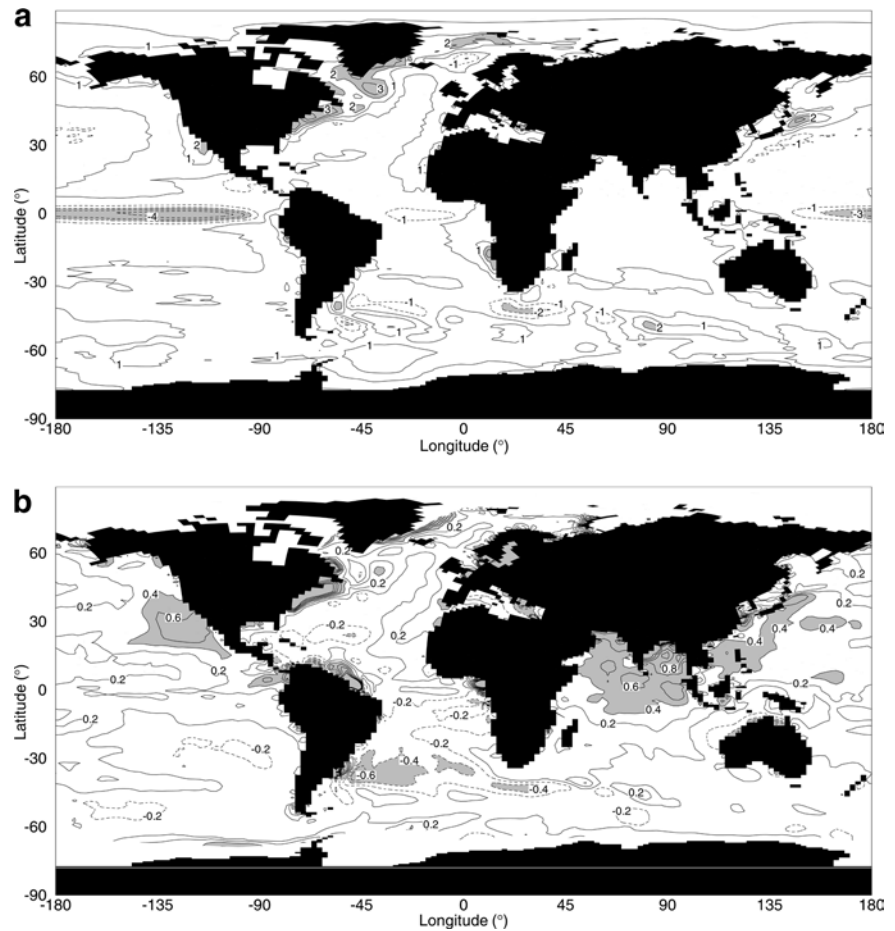


**Fig. 14** Mean T2m deviation from Jones 1961–1990 climatology (Jones 1994) for **a** DJF and **b** JJA. Contours are drawn at  $\pm 2$ , 5, 10 °C with deviation larger than 5 °C shaded. Solid line indicates that BCM is warmer than observed

Power spectra of the principal components (Fig. 19d) show that for frequencies less than 0.1 cycles per year (CPY), the BCM data seem to contain less power, while in the frequency band 0.3–1 CPY, there is more power in

**Fig. 15** **a** Mean SST deviation from Reynolds climatology (Reynolds and Smith 1994), and **b** mean SSS deviation from Levitus climatology (Levitus et al. 1994). For salinity, the area beneath the mean ice cover is left out since the Levitus data is not realistic in much of that area (Steele et al. 2001). The contour interval for SST is 1 °C with deviation larger than 2 °C is shaded, and for SSS 0.2 psu with deviation larger than 0.4 psu is shaded



BCM than in NCEP. It should further be noted that in BCM maximum power is found at a slightly higher frequency than in the NCEP data, respectively at 0.33 and 0.28 CPY (37 and 43 months periods).

A correlation between the monthly mean T2m and the mean SST in the Niño-3 region (area bounded by 150°W to 90°W, 5°S to 5°N) also suggests that the ENSO system is realistically represented in BCM (Fig. 20). Compared to the NCEP data, the tongue of warm water along the equator, associated with El Niño episodes, is slightly too narrow and stretches too far west in the model. This is a common problem in many AOGCMs (e.g., Collins et al. 2001). Apart from this discrepancy, the patterns found in BCM and NCEP show a good agreement, with negative anomalies to the west, north and south of the warm tongue, positive anomalies in the western part of the Indian Ocean and in the tropical Atlantic, and also areas of warm water west of the Alaska coast and in an isolated spot centred at 60°S in the Pacific. The standard deviation of the Niño-3 index in BCM is 1.24 °C, compared to the observed 0.84 °C in the NCEP data and 0.81 °C in the optimum interpolated SST data in COADS (Kaplan et al. 1997, 1998). The reason for the overestimation of the Niño-3 variability is not clear, however it may be related to a too coarse vertical resolution in the equatorial Pacific in the ocean model (Sect. 5.5). Due to the resolution

problem, the enhanced upwelling during La Niña conditions brings waters from too large depths to the surface, making the surface waters much colder than observed. During El Niño situations with less upwelling, the model will be closer to observations, and the overall effect will be an overestimation of the variability in the surface temperatures.

It is interesting to note the similarities of the spectra for low frequencies (Fig. 20d). Thus the larger Niño-3 SST variability is primarily due to more variability at the highest frequencies. The maximum is at a slightly higher frequency in BCM than in the NCEP data, a result consistent with that achieved from the SLP data and similar to that found in other models (e.g. Collins et al. 2001). The correlation between the SLP principal component and the Niño-3 index is for the BCM 0.63, compared to 0.53 for the NCEP data and 0.57 for the COADS data.

## 6.2 The NAO/AO mode

In Fig. 21 the winter (DJFM) mean SLP anomalies, regressed upon the principal component of the leading mode of winter mean SLP variability calculated for the region northwards of 20°N are shown for the BCM and NCEP data. The leading mode is the well known NAO/

**Fig. 16** Mean sea-ice thickness for **a,c** March and **b, d** September. The *white area* shows mean ice thickness above 0.01 m and contours are drawn at 0.1 m and then for each 0.5 m

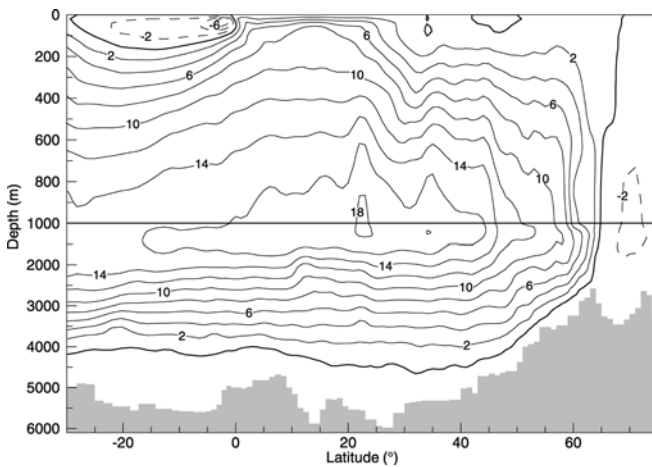
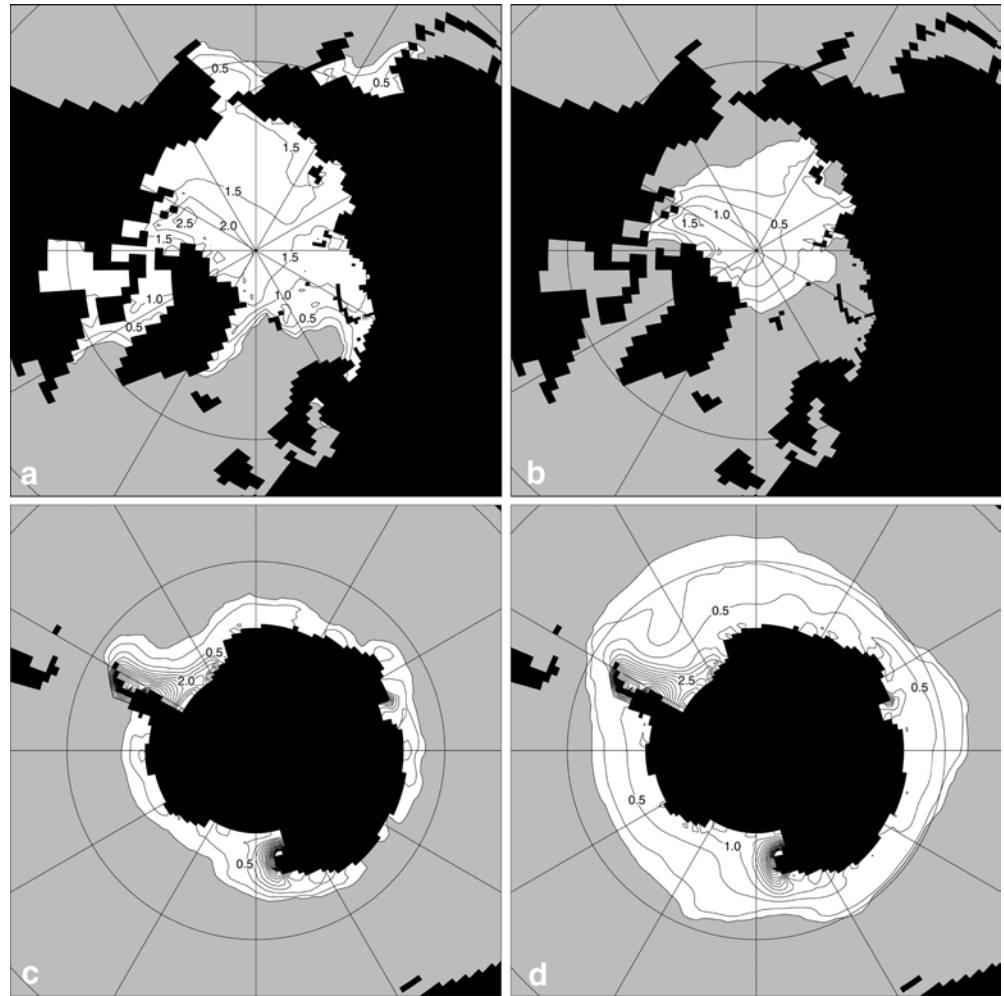


**Fig. 17** Atlantic meridional overturning stream function (Sv)

AO dipole pattern, where anomalous high pressure in the subtropics is associated with anomalous low pressure over the Nordic Seas and Arctic Ocean. The main discrepancy between the BCM and NCEP results is that the negative centre of action in the BCM is too far west, and does not have the pronounced trough into the Nordic

Seas seen in the NCEP data. This is consistent with the storm tracks being too zonal in this area (not shown). There is also a stronger teleconnection to the North Pacific in the BCM compared to the NCEP data. The mode explains 32% of the winter mean variability for both the BCM and NCEP data. For the leading mode calculated from the monthly means, the corresponding figure was 18%, again for both model and observations.

Compared to the ENSO signal which had a clear energy maximum near 0.3 CPY, the NAO signal has a white spectrum (Fig. 21d), with no significant differences between the BCM and the NCEP spectra.

The anomalous SLP field associated with the NAO/AO, has a large impact on the SST and surface air temperature in the North Atlantic region. Stephenson and Pavan (2002) compared the EOFs of the surface temperature in the region 120°W to 60°E, 20°N to 80°N for 17 climate models participating in the first phase of the coupled model intercomparison project (CMIP, Lambert and Boer 2001), showing large discrepancies between the models. Following their method, we first standardise the T2m time series in order to avoid giving the data over land too much weight (due to the difference in thermal properties between land and ocean), and

**Fig. 18** Mean stream function of vertically integrated mass transport. The contour interval is 10 Sv with positive values shaded

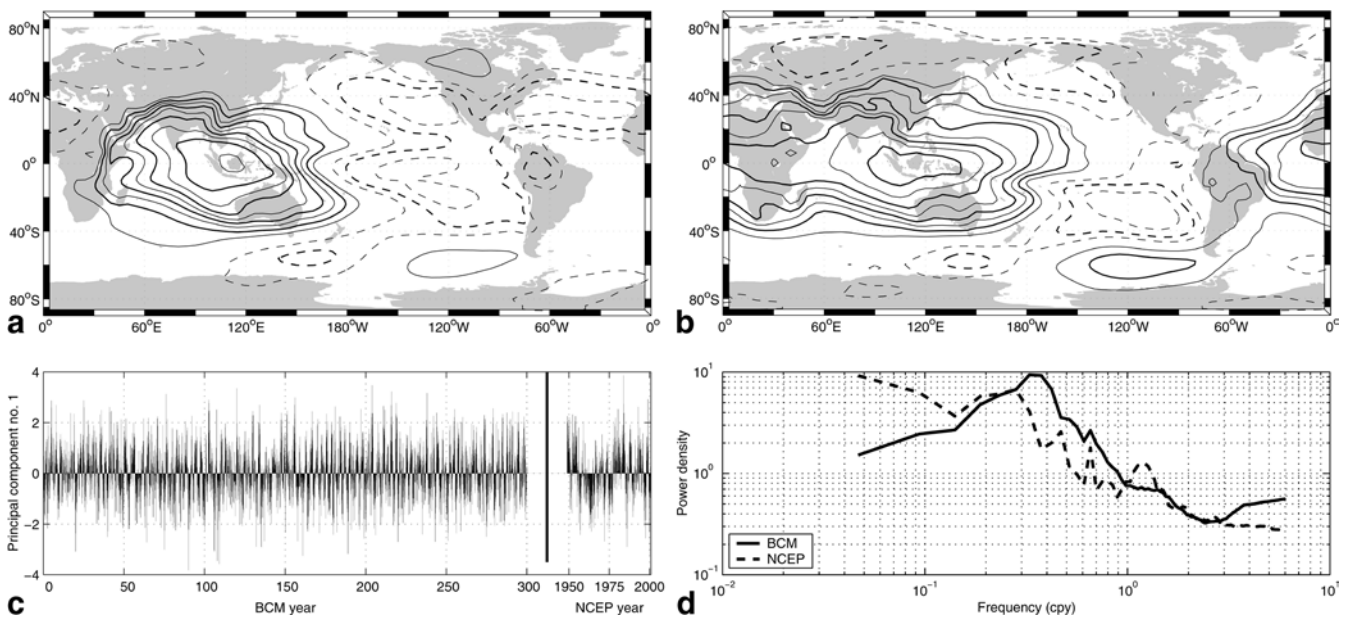
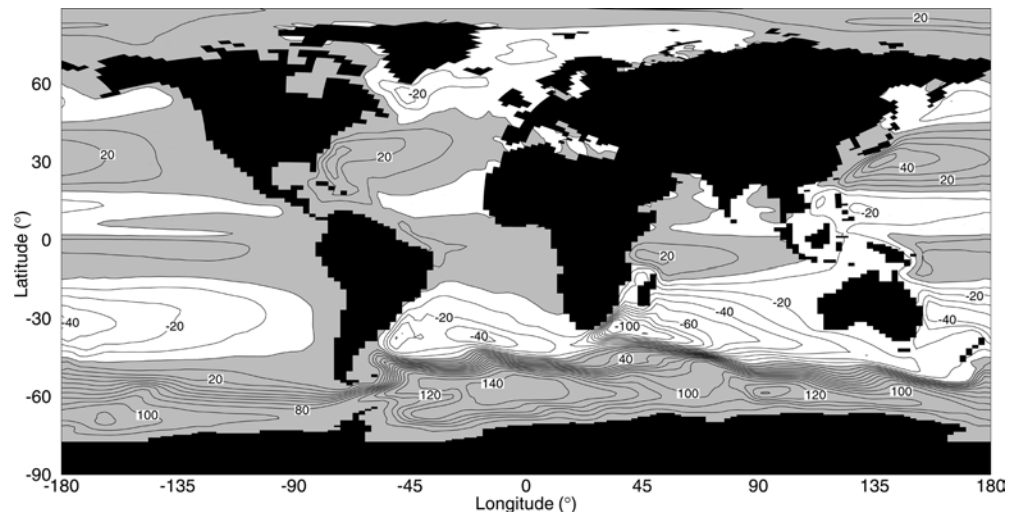


**Fig. 19** Upper panels show the correlation between the monthly mean global SLP field and the principal component of the leading mode of variability (1. EOF) of monthly mean SLP calculated over the area between 30°S and 30°N for a BCM and b NCEP. Contour

interval is 0.1 with negative contours dashed. The zero contour is not shown. Linear trends are removed prior to the calculations. Lower panels show the time series of the principal components for c BCM and NCEP, and d the power spectra for the same curves

otherwise perform the same analysis as for the SLP. The BCM fields have been compared both to the NCEP data, and to the monthly averaged Jones temperature data set from 1851 to present (Fig. 22). The latter data set is updated from the combined Jones (1994) land air temperature anomalies and the Parker et al. (1995) SST anomalies, and is given as anomalies relative to the 1961–1990 climatology on a  $5^\circ \times 5^\circ$  grid. All missing data points have here been assigned their climatological values prior to the EOF calculations.

Both for the calculations based on the winter means, and for the calculations based on all monthly means, the BCM gives a very good representation of the observed leading mode of T2m variability. The well known pattern

associated with the NAO is a quadrupole in temperature, with positive phase of the NAO (increased westerlies) associated with higher than normal temperatures centred over northern Europe and the southeastern part of the North America, and lower than normal temperatures centred over the Labrador Sea and the north-western Africa. For the monthly mean data, this pattern describes 10% of the variance in all three data sets, for the winter means it describes 20% in the BCM and NCEP data, and 16% in the Jones data set.

The spectra calculated from the three data sets tend to be red and have no preferred frequency, in contrast to the ENSO (Figs. 19d, 20d). However, there seems to be a local maximum between 0.3 and 0.4 CPY, close to the

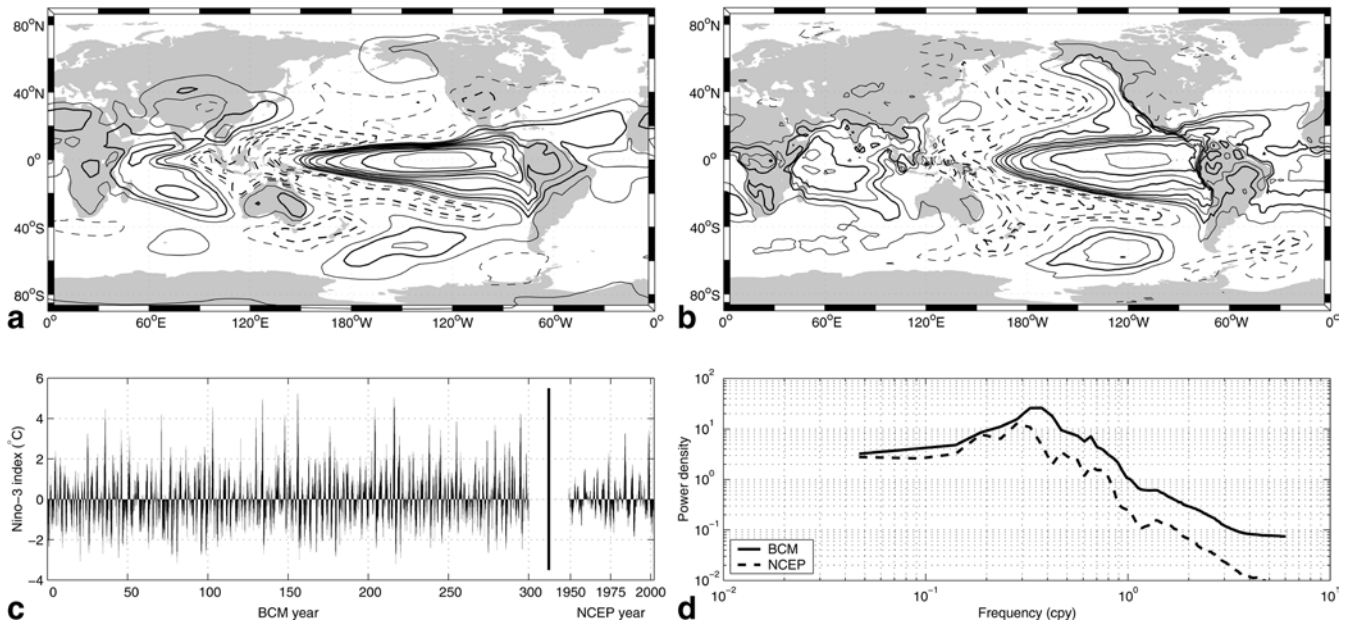


**Fig. 20** Upper panels show the correlation between the monthly mean global SST field and the Niño-3 index (average SST in the area 150°W to 90°W, 5°S to 5°N for **a** BCM) and **b** NCEP. Contour interval is 0.1, with negative contours *dashed*. The zero

contour is not shown. Linear trends are removed prior to the calculations. Lower panels show time series of the Niño-3 indices for **c** BCM and NCEP, and **d** the power spectra for the same curves

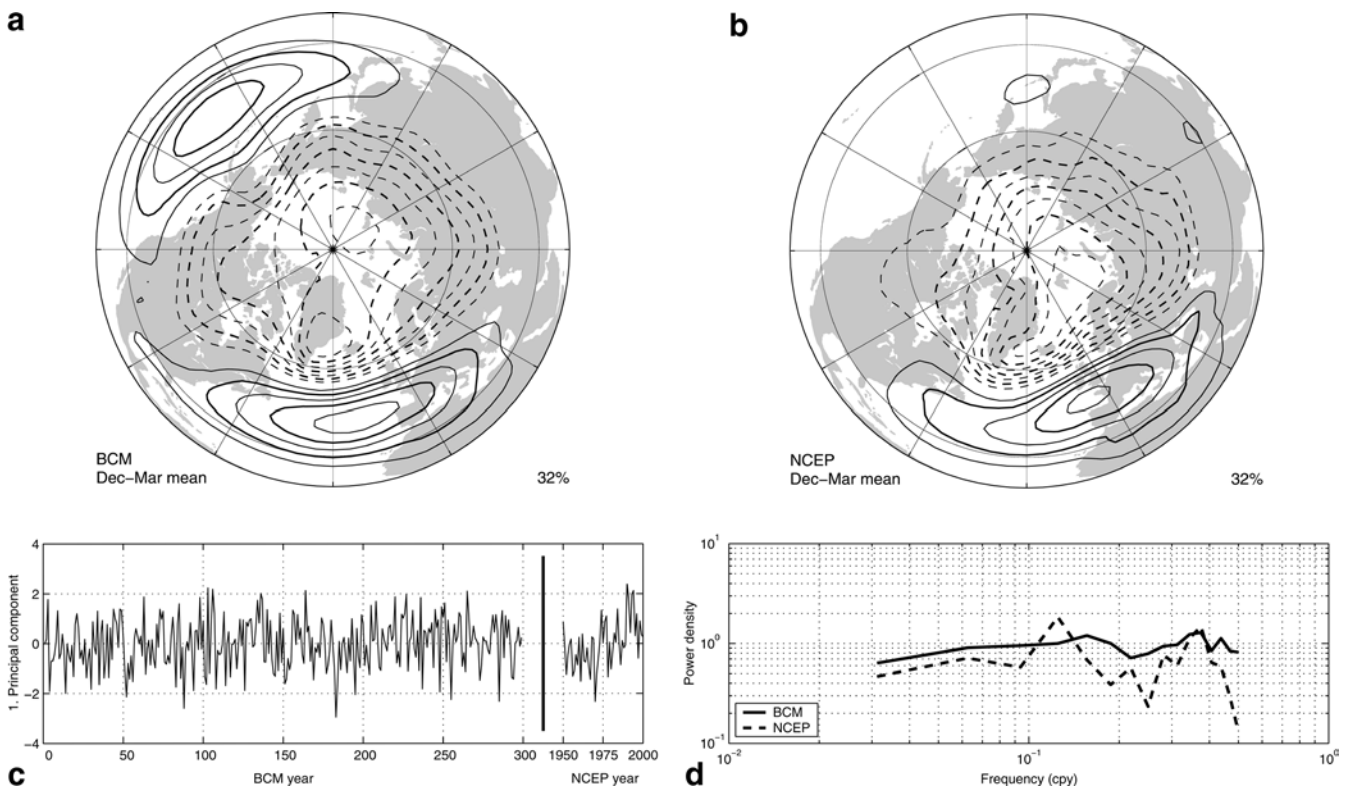


**Fig. 21** Upper panels show the winter (DJFM) mean global SLP field regressed on the principal component of the leading mode of variability (1. EOF) of the winter mean SLP calculated over the region poleward of 20°N for **a** BCM and **b** NCEP. Contour interval

is 0.25 mb, with negative contours *dashed*. The zero contour is not shown. Lower panels show the principal components for **c** BCM and NCEP and **d** the power spectra for the principal components

ENSO frequency. This may be due to an ENSO influence in the southwestern part of the analysis area. The energy in the spectra is strongly decreasing towards the

highest frequencies, a result of the thermal inertia of the ocean, as oceanic heat anomalies may be persistent on multi-monthly time scales. In contrast the spectra

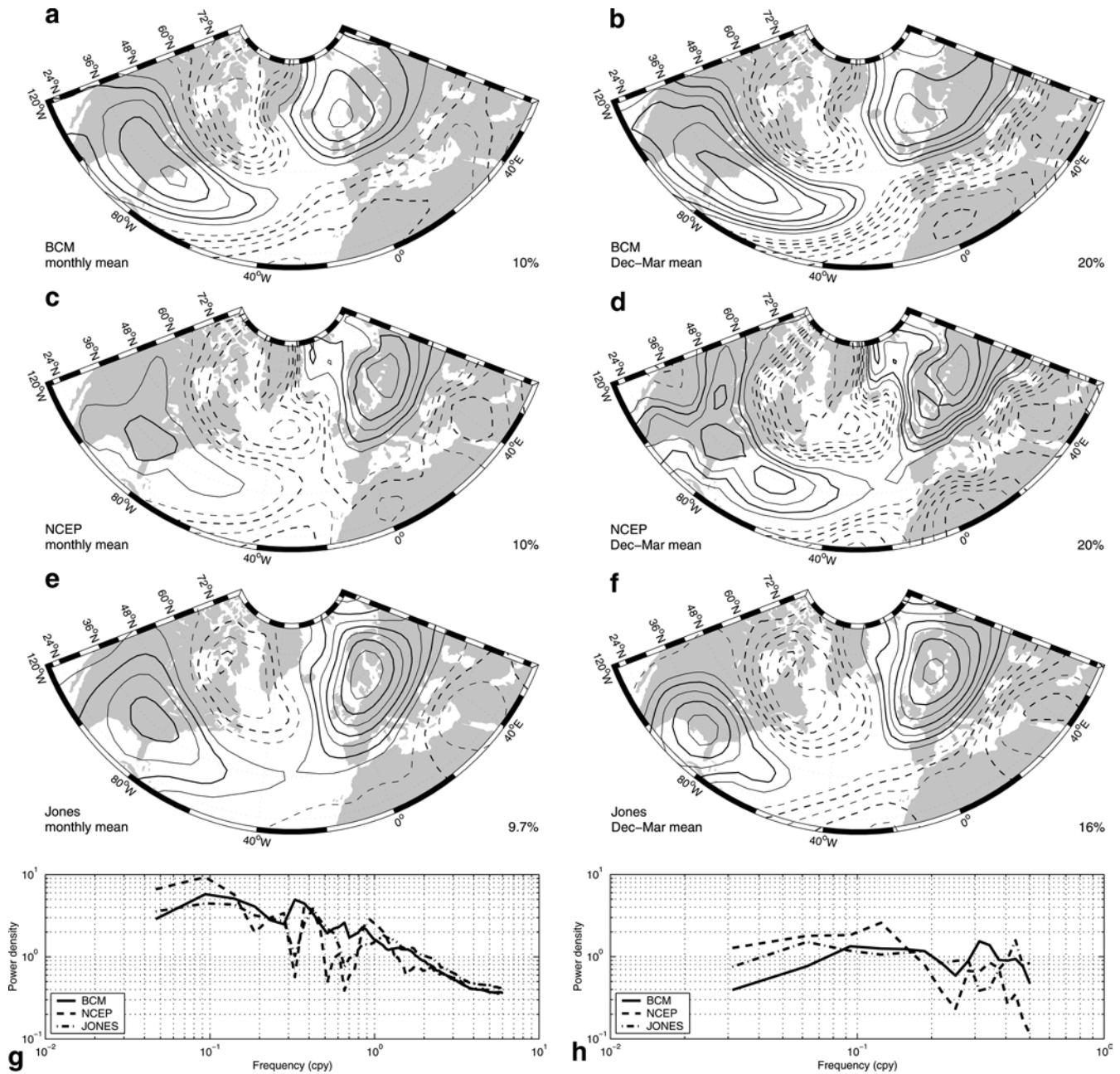


**Fig. 22** Upper panels show the T2m regressed on the leading mode of variability (1. EOF) for monthly (left) and winter (right) T2m calculated over the area 120°W to 60°E, 20°N to 80°N for BCM (first row), NCEP (middle row) and Jones (lower row). Contour

interval is 0.1 °C, with negative contours dashed. The zero contour is not shown. Lower panels show the power spectra for the principal components calculated for monthly means (left) and winter means (DJFM, right)

calculated from the monthly mean SLP data are almost flat at all frequencies.

The correlations between the first principal components calculated from the SLP and T2m data are 0.68 and 0.85 for the BCM and NCEP winter data, and 0.60 and 0.66 for the monthly data, respectively. Thus there is slightly weaker correlation between the SLP and T2m pattern in the BCM than what is found in the NCEP data.

## 7 Summary and discussion

Our main purpose has been to present the Bergen Climate Model (BCM), an AOGCM developed as a joint effort between the Geophysical Institute at the University of Bergen and the Nansen Environmental and Remote Sensing Center. The model system consists of the ARPEGE/IFS climate model, coupled to a global

version of the MICOM ocean model, the latter having a dynamic and thermodynamic sea-ice module implemented.

The motivation for coupling these two models is that they both handle variable horizontal grid spacing, so it will be possible to perform coupled model integration with both model components focused in certain areas. An obvious candidate for a focus area will be the North Atlantic–Arctic region, a key area for the deep water formation and thermohaline circulation, and a region having large variability both in the atmosphere and ocean. Other candidates for enhanced grid resolution are the tropical Pacific, Indian, and Atlantic Oceans. The approach of utilising global models with stretched grid systems is an alternative, dynamically consistent, approach to the standard dynamical downscaling. In the latter case, high-resolution regional model components are forced with boundary data from a coarse AOGCM simulation, and no information is passed from the regional to the global model.

For the 300-year integration presented, we have used an essential regular grid version of BCM for simulating present-day climate. The model has been analysed both for mean and transient climate. The model indeed captures the main features of the observed climate, and in particular the simulation of radiation, clouds, and freshwater fluxes is well produced. The model system is also realistic in simulating the oceanic 3-D circulation. For the large-scale variability, focus has been put on the ENSO and NAO/AO modes of variability. It is shown that BCM captures both these modes, and gives realistic frequency distributions and areas of influence.

The characteristics of the modest drift in the model indicate that a longer relaxation period to compute the flux adjustments, would have been more optimal. However, this will be examined in future experiments. Focus will also be on an attempt to improve the simulation of the equatorial upwelling, particularly in the Pacific Ocean, and in the treatment of sea ice. These will be highly prioritised tasks, as both the variability in the tropical Pacific and in the sea-ice distribution in the North Atlantic and Arctic region, may be key factors as far as regional climate simulations are concerned.

It is believed that the BCM configuration presented here forms the basis for many forthcoming studies of the global climate system in general, and the regional climate in particular.

**Acknowledgements** The authors are grateful to Laurent Terray at CERFACS, Toulouse, for the initial set-up of the OASIS coupler in Bergen, to Michel Déqué and David Salas Méliá, Météo-France, Toulouse, for providing technical assistance and support, and to Lennart Bengtsson, MPI, Hamburg, for a series of useful discussions and thorough guidance during the work. Constructive criticisms and suggestions made by Ronald J. Stouffer, GFDL, Princeton, during the review process, are greatly appreciated. The development of the Bergen Climate Model and the model integrations have received support from the Research Council of

Norway through the RegClim project, the “Spissforskningsmidler” (MB), and the Programme for Supercomputing. Additional funding has been received from the Board of Marine Sciences, University of Bergen, and the European Commission funded project PREDICATE (EVK2-CT-1999-00020) (HD). This is contribution A0013 from the Bjerknes Centre for Climate Research.

## Appendix 1

### 1.1 Computation of sea-ice surface temperature

The thermodynamic component of the sea-ice model has one ice layer and one snow layer. The temperature is determined at the ice-snow and the snow-air boundaries, assuming linear temperature profiles in the interior of the ice and snow, and with the freezing temperature of sea water as a boundary condition at the bottom of the ice. The temperatures are then diagnosed by balancing the heat flux budget at the snow-air boundary.

If only the situation with ice and no snow is considered, the heat balance at the top of ice can be stated as:

$$k \frac{\partial T}{\partial z} \Big|_{h_{\text{ice}}} + Q_{\text{ns}} + Q_{\text{sw}} = 0, \quad (3)$$

where  $k$  is ice conductivity,  $T$  is temperature in the ice,  $h_{\text{ice}}$  is ice thickness,  $Q_{\text{ns}}$  is non-solar heat flux, and  $Q_{\text{sw}}$  is solar heat flux. The non-solar heat flux depends on the surface temperature  $T_s$  and is updated in the atmosphere model using the temperature of the previous time step

$$Q_{\text{ns}}^n = Q_{\text{ns}}(T_s^{n-1}). \quad (4)$$

Here  $n$  denotes the coupling time step. Assuming a linear temperature profile through the ice gives

$$k \frac{T_s - T_f}{h_{\text{ice}}} + Q_{\text{ns}} + Q_{\text{sw}} = 0, \quad (5)$$

where  $T_f$  is the freezing temperature of sea water. Solving for  $T_s^{n+1}$  using heat fluxes from time step  $n$  leads to an unstable time step procedure. To remedy this,  $Q_{\text{ns}}$  can be linearised around  $T_s$  to approximate the non-solar flux at  $n + 1$ :

$$\tilde{Q}_{\text{ns}}^{n+1} \approx Q_{\text{ns}}^n + \frac{\partial Q_{\text{ns}}^n}{\partial T_s} (T_s^{n+1} - T_s^n). \quad (6)$$

A stable updating of  $T_s$  is obtained from

$$k \frac{T_s^{n+1} - T_f}{h_{\text{ice}}} + \tilde{Q}_{\text{ns}}^{n+1} + Q_{\text{sw}} = 0, \quad (7)$$

The term  $\partial Q_{\text{ns}}^n / \partial T_s$ , delivered from the atmosphere model, is also used by the coupler to modify the distribution of non-solar heat fluxes received by ocean cells covered by the same atmosphere cell (see Sect. 3).

## References

- Ardanuy PE, Stowe LL, Gruber A (1991) Shortwave, longwave and net cloud radiative forcing as determined from Nimbus-7 observations. *J Geophys Res* 96: 18,537–18,549
- Barkstrom BR (1984) The Earth Radiation Budget Experiment (ERBE). *Bull Am Meteorol Soc* 65: 1170–1185
- Barnard S et al. (1997) DYNAMO – Dynamics of North Atlantic models: simulation and assimilation with high resolution models. Tech Rep 294 Inst. Meereskunde, Christian Albrechts Universität, Kiel, Germany
- Barthelet P, Terray L, Valcke S (1998) Transient CO<sub>2</sub> experiment using the ARPEGE/OPAICE non flux corrected coupled model. *Geophys Res Lett* 25: 2277–2280
- Baumgartner A, Reichel E (1975) The world water balance. R. Oldenbourg, Munich, Germany, pp 179
- Beesley JA, Moritz RE (1999) Toward an explanation of the annual cycle of cloudiness over the Arctic Ocean. *J Clim* 12: 395–415

- Bentsen M, Drange H (2000) Parameterizing surface fluxes in ocean models using the NCEP/NCAR reanalysis data. In: RegClim General Techn Rep 4, pp 149–158. Norwegian Institute for Air Research, Kjeller, Norway
- Bentsen M, Evensen G, Drange H, Jenkins AD (1999) Coordinate transformation on a sphere using conformal mapping. *Mon Weather Rev* 127: 2733–2740
- Bjørge E, Johannessen OM, Miles MW (1997) Analysis of merged SMMR-SSM/I time series of Arctic and Antarctic sea ice parameters 1978–1995. *Geophys Res Lett* 24: 413–416
- Bleck R, Rooth C, Hu D, Smith LT (1992) Salinity-driven thermocline transients in a wind- and thermohaline-forced isopycnic coordinate model of the North Atlantic. *J Phys Oceanogr* 22: 1486–1505
- Boone A, Masson V, Meyers T, Noilhan J (2000) The influence of the inclusion of soil freezing on simulations by a soil-vegetation-atmosphere transfer scheme. *J Appl Meteor* 39: 1544–1569
- Bossuet C, Déqué M, Cariolle D (1998) Impact of a simple parameterization of convective gravity-wave drag in a stratosphere-troposphere general circulation model and its sensitivity to vertical resolution. *Ann Geophysicae* 16: 238–249
- Bougeault P (1985) A simple parameterization of the large-scale effects of deep cumulus convection. *MWR* 113: 2108–2121
- Bourke RH, McLaren AS (1992) Contour mapping of arctic basin ice draft and roughness parameters. *J Geophys Res* 97: 17,715–17,728
- Cariolle D, Déqué M (1986) Southern hemisphere medium-scale waves and total ozone disturbances in a spectral general circulation model. *J Geophys Res* 91: 10,825–10,846
- Cassou C, Noyret P, Sevault E, Thual O, Terray L, Beaucourt D, Imbard M (1998) Distributed ocean–atmosphere modelling and sensitivity to the coupling flux precision: the CATHODE Project. *Mon Weather Rev* 126: 1035–1053
- Coiffier J, Ernie Y, Geleyn JF, Clochard J, Hoffman J, Dupont F (1987) The operational hemispheric model at the French Meteorological Service. In: *J Meteorol Soc Japan, Special NWP Symposium Vol pp 337–345*
- Collins M, Tett SFB, Cooper C (2001) The internal climate variability of HadCM3, a version of the Hadley Centre coupled model without flux adjustment. *Clim Dyn* 17: 61–81
- Courtier P, Freyrier C, Geleyn JF, Rabier F, Rochas M (1991) The ARPEGE project at Météo-France. In: *Proc ECMWF workshop on numerical methods in atmospheric modelling 2: 193–231*. ECMWF
- Covey CC, AchutaRao KM, Lambert SJ, Taylor KE (2000) Intercomparison of present and future climates simulated by coupled ocean–atmosphere GCMs. PCMDI Report Series 66 Lawrence Livermore National Laboratory, pp 52
- da Silva AM, Young CC, Levitus S (1994) Atlas of surface marine data 1994, Volumes 1 and 3. NOAA Atlas NESDIS 6 and 8, US Department of Commerce, Washington, D.C. pp 83
- Darnell WL, Staylor WF, Gupta SK, Ritchey NA, Wilber AC (1992) Seasonal variation of surface radiation budget derived from ISCCP-C1 data. *J Geophys Res* 97: 15,741–15,760
- Déqué M, Piedelievre JP (1995) High resolution climate simulation over Europe. *Clim Dyn* 11: 321–339
- Déqué M, Dreveton C, Braun A, Cariolle D (1994) The ARPEGE/IFS atmosphere model: a contribution to the French community climate modelling. *Clim Dyn* 10: 249–266
- Déqué M, Marquet P, Jones RG (1998) Simulation of climate change over Europe using a global variable resolution general circulation model. *Clim Dyn* 14: 173–189
- Dorman CE, Bourke RH (1978) Temperature correction for Tucker's ocean rainfall estimates. *Q J R Meteorol Soc* 104: 765–773
- Douville H, Royer JF, Mahfouf JF (1995) A new snow parameterization for the Météo-France climate model. Part II: validation in a 3D GCM experiment. *Clim Dyn* 12: 37–52
- Drange H (1999) RegClim ocean modelling at NERSC. In: *RegClim General Technical Report 2*, pp 93–102. Norwegian Institute for Air Research, Kjeller, Norway
- Drange H, Simonsen K (1996) Formulation of Air–Sea Fluxes in the ESOP2 Version of MICOM. Technical Report 125 Nansen Environmental and Remote Sensing Center, Bergen, Norway, pp 23
- Fichefet T, Gaspar P (1988) A model study of upper ocean–sea ice interaction. *J Phys Oceanogr* 18: 181–195
- Flato GM, Boer GJ, Lee WG, McFarlane NA, Ramsden D, Reader MC, Weaver AJ (2000) The Canadian Centre for Climate Modelling and Analysis global coupled model and its climate. *Clim Dyn* 16: 451–467
- Gal-Chen T, Somerville RCJ (1975) On the use of a coordinate transformation for the solution of the Navier-Stokes equations. *J Comput Phys* 17: 209–228
- Ganopolski A, Rahmstorf S (2001) Rapid changes of glacial climate simulated in an coupled climate model. *Nature* 409: 153–158
- Gaspar P (1988) Modeling the seasonal cycle of the upper ocean. *J Phys Oceanogr* 18: 161–180
- Geleyn JF (1987) Use of a modified Richardson number for parameterizing the effect of shallow convection. In: *J Met Soc Japan, Special NWP Symposium*, pp 141–147
- Geleyn JF (1988) Interpolation of wind, temperature and humidity values from model levels to the height of measurement. *Tellus* 40A: 347–351
- Geleyn JF, Preuss HJ (1983) A new dataset of satellite derived surface albedo values for operational use at ECMWF. *Arch Meteorol Geophys Biocl, Ser A* 32: 353–359
- Gordon C, Cooper C, Senior CA, Banks H, Gregory JM, Johns TC, Mitchell JFB, Wood RA (2000) The simulation of SST, sea ice extents and ocean heat transports in a version of the Hadley Centre coupled model without flux adjustments. *Clim Dyn* 16: 147–168
- Gordon HB, O'Farrell SP (1997) Transient climate change in the CSIRO coupled model with dynamic sea ice. *Mon Weather Rev* 125: 875–907
- Gouillyard E, Madec G (1997) Performance of the OPA/ARPEGE-T21 global ocean–atmosphere coupled model. *Clim Dyn* 13: 149–165
- Harder M (1996) Dynamik, Rauigkeit und Alter des Meereises in der Arktis. PhD thesis Alfred-Wegener-Institut für Polar- und Meeresforschung, Bremerhaven, Germany, pp 124
- Harrison EF, Minnis P, Barkstrom BR, Ramanathan V, Cess RD, Gibson GG (1990) Seasonal variation of cloud radiative forcing derived from the Earth Radiation Budget Experiment. *J Geophys Res* 95: 18,687–18,703
- Hibler III WD (1979) A dynamic thermodynamic sea ice model. *J Phys Oceanogr* 9: 815–846
- Hines KM, Bromwich DH, Marshall GJ (2000) Artificial surface pressure trends in the NCEP-NCAR reanalysis over the Southern Ocean and Antarctica. *J Clim* 13: 3940–3952
- Hortal M (1998) Aspects of the numerics of the ECMWF model. In: *Proc Recent developments in numerical methods for atmospheric modelling, ECMWF*, pp 127–143
- Hortal M, Simmons AJ (1991) Use of reduced Gaussian grids in spectral models. *Mon Weather Rev* 119: 1057–1074
- Huffman GJ, Adler RF, Rudolf B, Schneider U, Keehn PR (1995) Global precipitation estimates based on a technique for combining satellite-based estimates, rain gauge analysis, and NWP model precipitation information. *J Clim* 8: 1284–1295
- Hurrell JW (1995) Decadal trends in the North Atlantic Oscillation: regional temperatures and precipitation. *Science* 269: 676–679
- Johannessen OM, Shalina EV, Miles MW (1999) Satellite evidence for an Arctic sea ice cover in transformation. *Science* 286: 1937–1939
- Johns TC, Carnell RE, Crossley JF, Gregory JM, Mitchell JFB, Senior CA, Tett SFB, Wood RA (1997) The second Hadley Centre coupled ocean–atmosphere GCM: model description, spinup and validation. *Clim Dyn* 13: 103–134
- Jones PD (1994) Hemispheric surface air temperature variations: a reanalysis and an update to 1993. *J Clim* 7: 1784–1802

- Kalnay E et al. (1996) The NCEP/NCAR 40-Year Reanalysis Project. *Bull Am Meteor Soc* 77: 437–471
- Kaplan A, Kushnir Y, Cane MA, Blumenthal MB (1997) Reduced space optimal analysis for historical datasets: 136 years of Atlantic sea surface temperatures. *J Geophys Res* 102: 27,835–27,860
- Kaplan A, Cane MA, Kushnir Y, Clement AC, Blumenthal MB, Rajagopalan B (1998) Analyses of global sea surface temperature 1856–1991. *J Geophys Res* 103: 18,567–18,589
- Kaplan A, Kushnir Y, Cane M (2000) Reduced space optimal analysis of historical marine sea level pressure: 1854–1992. *J Clim* 13: 2987–3002
- Kiehl JT, Trenberth KE (1997) Earth's annual global mean energy budget. *Bull Am Meteorol Soc* 78: 197–208
- Kiehl JT, Hack JJ, Briegleb BP (1994) The simulated earth radiation budget of the National Center for Atmospheric Research community climate model CCM2 and comparison with the Earth Radiation Budget Experiment (ERBE). *J Geophys Res* 99: 20,815–20,827
- Kraus EB, Turner JS (1967) A one-dimensional model for the seasonal thermocline. II The general theory and its consequences. *Tellus* 14: 98–105
- Lambert SJ, Boer GJ (2001) CMIP1 evaluation and intercomparison of coupled climate models. *Clim Dyn* 17: 83–106
- Levitus S, Boyer TP (1994) World Ocean Atlas 1994 volume 4: temperature. NOAA Atlas NESDIS 4, US Department of Commerce, Washington, D.C, pp 117
- Levitus S, Burgett R, Boyer TP (1994) World Ocean Atlas 1994 volume 3: salinity. NOAA Atlas NESDIS 3, US Department of Commerce, Washington, D.C, pp 99
- Lott F (1999) Alleviation of stationary biases in a GCM through a mountain drag parameterization scheme and a simple representation of mountain lift forces. *Mon Weather Rev* 125: 788–801
- Lott F, Miller MJ (1997) A new subgrid-scale orographic drag parameterization: its formulation and testing. *Q J R Meteorol Soc* 123: 101–127
- Louis JF (1979) A parametric model of vertical eddy fluxes in the atmosphere. *Boundary-Layer Meteorol* 17: 187–202
- Maded G, Imbard M (1996) A global ocean mesh to overcome the North Pole singularity. *Clim Dyn* 12: 381–388
- Mahfouf JF, Manzi AO, Noilhan J, Giordani H, Déqué M (1995) The land surface scheme ISBA within the Météo-France climate model ARPEGE. Part I: implementation and preliminary results. *J Clim* 8: 2039–2057
- Mantoura RFC, Martin JM, Wollast R (eds) (1991) Ocean margin processes in global change vol 9, Physical, chemical and earth sciences research Report. John Wiley Chichester, UK pp 486
- Mascart P, Noilhan J, Giordani H (1995) A modified parameterization of flux profile relationships in the surface layer using different roughness length values for heat and momentum. *Boundary-Layer Meteorol* 72: 331–344
- Miller AJ, Lermusiaux PFJ, Poulain PM (1996) A topographic-Rossby mode resonance over the Iceland-Faeroe Ridge. *J Phys Oceanogr* 26: 2735–2747
- Morcrette JJ (1991) Radiation and cloud radiative properties in the European Centre for Medium Range Forecasts forecasting system. *J Geophys Res* 95: 9121–9132
- Noilhan J, Planton S (1989) A simple parameterization of land surface processes for meteorological models. *Mon Weather Rev* 117: 536–549
- Oberhuber JM (1988) An atlas based on the 'COADS' data set: the budgets of heat, buoyancy and turbulent kinetic energy at the surface of the global ocean. Tech Rep 15 Max-Planck-Institut für Meteorologie, Hamburg, Germany
- Ohmura A, Gilgen H (1993) Re-evaluation of the global energy balance. In: Interactions between the global climate subsystems: the legacy of Hann, vol 75, pp 93–110. American Geophysical Union
- Oki T, Sud YC (1998) Design of total run off integrating pathways (TRIP): a global river channel network. *Earth interactions* vol 2, No. 1, pp 1–37
- Palmer TN (2001) A nonlinear dynamical perspective on model error: a proposal for non-local stochastic-dynamic parameterization in weather and climate prediction models. *Q J R Meteorol Soc* 127: 279–304
- Palmer TN, Räisänen J (2002) Quantifying the risk of extreme seasonal precipitation events in a changing climate. *Nature* 415: 512–514
- Paltridge GW, Platt CMR (1976) Radiative processes in meteorology and climatology. Elsevier, Amsterdam, pp 318
- Parker DE, Folland CK, Jackson M (1995) Marine surface temperature: observed variations and data requirements. *Clim Change* 31: 559–600
- Parkinson CL, Washington WM (1979) A large-scale numerical model of sea ice. *J Geophys Res* 84: 311–337
- Parkinson CL, Cavalieri DJ, Gloersen P, Zwally HJ, Comiso JC (1999) Arctic sea ice extents, areas, and trends, 1978–1996. *J Geophys Res* 104: 20,837–20,856
- Payne RE (1972) Albedo of the sea surface. *J Atmos Sci* 29: 959–970
- Rahmstorf S (1995) Bifurcations of the Atlantic thermohaline circulation in response to changes in the hydrological cycle. *Nature* 378: 145–149
- Rahmstorf S, Ganopolski A (1999) Long-term global warming scenarios computing with an efficient coupled climate model. *Clim Change* 43: 353–367
- Ramanathan VRD, Subasilar B, Zhang GJ, Contant W, Cess RD, Kiehl JT, Grassl H, Shi L (1995) Warm pool heat budget and shortwave cloud forcing: a missing physics? *Science* 267: 499–503
- Read JF, Pollard RT (1993) Structure and transport of the Antarctic circumpolar current and Agulhas return current at 40°E. *J Geophys Res* 98: 12,281–12,295
- Reynolds RW, Smith TM (1994) Improved global sea surface temperature analysis using optimum interpolation. *J Clim* 7: 929–948
- Richard JL, Royer JF (1993) A statistical cloud scheme for use in an AGCM. *Ann Geophysicae* 11: 1093–1115
- Rieland M, Raschke E (1999) Diurnal variability of the earth radiation budget: sampling requirements, time integration aspects and error estimates for the Earth Radiation Budget Experiment (ERBE). *Theor Appl Climatol* 44: 9–24
- Roekner E, Oberhuber JM, Bacher A, Christoph M, Kirchner I (1996) ENSO variability and atmospheric response in a global coupled atmosphere ocean GCM. *Clim Dyn* 12: 737–754
- Rossow WB, Schiffer RA (1991) ISCCP cloud data products. *Bull Am Meteorol Soc* 72: 2–20
- Rossow WB, Zhang YC (1995) Calculation of surface and top-of-atmosphere radiative fluxes from physical quantities based on ISCCP datasets: 2. Validation and first results. *J Geophys Res* 100: 1167–1197
- Rothrock DA, Yu Y, Maykut GA (1999) Thinning of the Arctic sea-ice Cover. *Geophys Res Lett* 26: 3469–3472
- Russel GL, Miller JR, Rind D (1995) A coupled atmosphere–ocean model for transient climate change studies. *Atmos–Ocean* 33: 683–730
- Semtner Jr. AJ (1976) A model for the thermodynamic growth of sea ice in numerical investigations of climate. *J Phys Oceanogr* 6: 379–389
- Shea DJ (1986) Climatological Atlas: 1950–1979 surface air temperature, precipitation, sea-level pressure, and sea-surface temperature (45°S–90°N). Tech Rep NCAR/TN-269+STR National Center for Atmospheric Research, Boulder, CO, USA
- Simmons AJ, Burridge DM (1981) An energy and angular momentum conserving vertical finite-difference scheme and hybrid vertical coordinate. *Mon Weather Rev* 109: 758–768
- Steele M, Morley R, Ermold W (2001) PHC: a global ocean hydrography with a high-quality Arctic Ocean. *J Clim* 14: 2079–2087
- Stephenson DB, Pavan V (2002) How well do climate models simulate the North Atlantic Oscillation? *Clim Dyn*. in press
- Sun S, Bleck R, Rooth C, Dukowicz J, Chassignet E, Killworth P (1999) Inclusion of Thermobaricity in Isopycnic-Coordinate Ocean Models. *J Phys Oceanogr* 29: 2719–2729
- Terray L, Thual O (1995) Oasis: le couplage océan–atmosphère. *La Météorologie* 10: 50–61

- Terray L, Thual O, Belamari S, Déqué M, Dandin P, Lévy C, Delecluse P (1995) Climatology and interannual variability simulated by the ARPEGE-OPA model. *Clim Dyn* 11: 487–505
- Terray L, Valcke S, Piacentini A (1998) OASIS 2.2. User's guide and reference manual. Tech Rep CERFACS, Toulouse, France, pp 77
- Tucker GB (1961) Precipitation over the North Atlantic Ocean. *Q J R Meteorol Soc* 87: 147–158
- Wadhams P, Davis NR (2000) Further evidence of ice thinning in the Arctic Ocean. *Geophys Res Lett* 27: 3973–3976
- Walsh JE, Chapman WL, Shy TL (1996) Recent decrease of sea level pressure in the central Arctic. *Notes and Correspondence. J Climate* 9: 480–486
- Whitlock CH, Charlock TP, Staylor WF, Pinker RT, Laszlo I, Ohmura A, Gilgen H, Konzelman T, Pasquale RCD, Moats CD, LeCroy SR, Ritchey NA (1995) First global WCRP shortwave surface radiation budget data set. *Bull Am Meteorol Soc* 76: 905–922
- Woodruff SD, Slutz RJ, Jenne RL, Steurer PM (1987) A comprehensive ocean-atmosphere data set. *Bull Am Meteorol Soc* 68: 1239–1250
- Xie P, Arkin PA (1997) Global precipitation: A/17-year monthly analysis based on gauge observations, satellite estimates, and numerical model outputs. *Bull Am Meteorol Soc* 78: 2539–2558